

Aalto University
School of Electrical Engineering
Master's Programme in Life Science Technologies

Kirsi Toivonen

Reduction of Baseline Wander in Electrocardiography Using Kalman Filters

Master's Thesis
Espoo, May 25, 2020

Supervisor:	Prof. Ivan Vujaklija
Advisor:	Prof. Simo Särkkä

Author:	Kirsi Toivonen		
Title:	Reduction of Baseline Wander in Electrocardiography Using Kalman Filters		
Date:	May 25, 2020	Pages:	vii + 54
Major:	Biosensing and Bioelectronics	Code:	ELEC3045
Supervisor:	Prof. Ivan Vujaklija		
Advisor:	Prof. Simo Särkkä		
<p>Developments in sensor technology have enabled the continuous electrocardiography monitoring during daily activities. These recordings can be valuable in the detection of arrhythmias and abnormal cardiac cycles that occur only under certain circumstances or infrequently. Unfortunately, the activities of the patient cause severe motion artifacts to the ECG signal that affect the signal quality and complicate the signal interpretation. The motion based baseline wander artifact can be reduced to a certain point by improving the stability of the electrode-skin interface. However, also computational signal processing methods, like adaptive filtering, are needed. The signal processing methods can be improved by utilizing additional variables that correlate with the artifact sources. For example, acceleration and impedance signals have been studied as possible references of motion. However, being able to do the measurements without additional sensors would enable the measurement device to be simpler, lighter, and lower in cost.</p> <p>This thesis presents an accelerometer-free ECG signal baseline wander reduction algorithm that uses electromyography signal as a Kalman filter reference signal. The EMG signal is extracted from the ECG signal itself and used as an estimate of local electrode motion. The motion estimate is then used as a reference signal for an adaptive Kalman filter baseline wander compensation algorithm. The algorithm is evaluated on data collected in clinical trials. In addition, the feasibility of removing the baseline wander using a reduced number of accelerometers as a motion reference for Kalman filter is studied.</p> <p>The results showed that the proposed method removed baseline wander successfully and without significant alterations in the signal morphology. The method proved to be at least equally proficient with the methods it was compared to. The results suggested that the baseline wander reduction from ambulatory ECG measurements could be achieved without additional sensors using EMG signal as a motion reference for the Kalman filter. In addition, also the reduced number of accelerometers proved to be a feasible source of the motion reference signal.</p>			
Keywords:	electrocardiography, Kalman filter, baseline wander, signal processing, artifact reduction		
Language:	English		

Tekijä:	Kirsi Toivonen		
Työn nimi:	Perustason vaellushäiriön vähentäminen elektrokardiografiassa Kalman-suotimilla		
Päiväys:	25. toukokuuta 2020	Sivumäärä:	vii + 54
Pääaine:	Biosensing and Bioelectronics	Koodi:	ELEC3045
Valvoja:	Prof. Ivan Vujaklija		
Ohjaaja:	Prof. Simo Särkkä		
<p>Sensoriteknologian kehitys on mahdollistanut sydänsähkökäyrän jatkuvan mittaamisen päivittäisten aktiviteettien aikana. Jatkuvat mittaukset voivat auttaa havaitsemaan sellaisia rytmihäiriöitä ja epänormaaleja sydämen toimintakiertoja, jotka esiintyvät vain tietyissä olosuhteissa tai epäsäännöllisesti. Potilaan liikkeet kuitenkin aiheuttavat sydänsähkökäyrään voimakkaita liikeartefakteja, jotka heikentävät signaalin laatua ja vaikeuttavat signaalin tulkintaa. Liikkeestä aiheutuvaa perustason vaellushäiriötä voidaan hieman vähentää parantamalla ihon ja elektrodin välisen rajapinnan vakautta. Kuitenkin myös laskennallisia signaalinkäsittelymenetelmiä, kuten adaptiivisia suotimia, tarvitaan. Signaalinkäsittelymenetelmiä voidaan tehostaa hyödyntämällä lisämittaussuureita, jotka korreloivat artefaktien lähteen kanssa. Esimerkiksi kiihtyvyys- ja impedansisignaaleja on tutkittu mahdollisina liikereferensseinä.</p> <p>Tässä diplomityössä ehdotetaan perustason vaellushäiriön vähentämiseen sydänsähkökäyrästä menetelmää, joka ei hyödynnä lisäensoreita, vaan käyttää lihassähkökäyrää Kalman-suotimen liike-estimaattina. Lihassähkökäyrä erotetaan sydänsähkökäyrästä ja sitä käytetään estimaattina elektrodien paikallisesta liikkeestä. Liike-estimaattia puolestaan hyödynnetään adaptiiviseen Kalman-suotimeen perustuvan perustason vaellushäiriön kompensatioalgoritmin referenssisignaalina. Algoritmi arvioidaan kliinisissä kokeissa kerätyllä datalla. Lisäksi tutkitaan Kalman-suotimen toimivuutta käytettäessä pienempää määrää kiihtyvyysantureita liike-estimaatin lähteenä.</p> <p>Tulokset osoittivat, että ehdotettu menetelmä poisti onnistuneesti perustason vaellushäiriön muuttamatta signaalin muotoa merkittävästi. Ehdotettu menetelmä osoittautui toimivan vähintään yhtä hyvin kuin menetelmät, joihin sitä verrattiin. Tulosten mukaan perustason vaellushäiriön vähentäminen liikkeen aikaisista sydänsähkökäyrämittauksista olisi mahdollista ilman lisäensoreita käyttämällä lihassähkökäyrää Kalman-suotimen liikereferenssinä. Lisäksi, vähennetty määrä kiihtyvyysantureita osoittautui myös toimivaksi liike-estimaatin lähteeksi.</p>			
Asiasanat:	elektrokardiografia, Kalman-suodin, perustason vaellushäiriö, signaalinkäsittely, artefaktien vähentäminen		
Kieli:	Englanti		

Acknowledgements

First, I would like to express my deepest appreciation to my supervisor Professor Ivan Vujaklija for his guidance and support throughout this thesis process. I always left the meetings with a bit more belief in my work and in myself. I also wish to thank my advisor Professor Simo Särkkä for providing me with the opportunity to work on this interesting topic. I would also like to acknowledge the help provided by Roland Hostettler, Tuomas Lumikari and Lauri Palva.

I am extremely grateful to my parents for encouraging me to follow my interests in my studies and in life in general. I would also like to thank my sisters for their unwavering support and for being such great role models.

Finally, I would like to thank Petter for his invaluable support, encouragement and patience. Thank you for reminding me to keep things in perspective.

Espoo, May 25, 2020

Kirsi Toivonen

Abbreviations and Acronyms

AV	Atrioventricular
DOF	Degrees of freedom
ECG	Electrocardiography
EMG	Electromyography
ENU	East-north-up
FFT	Fast Fourier transform
IIR	Infinite impulse response
IMU	Inertial measurement unit
KL	Kullback–Leibler
PSD	Power spectral density
RMSE	Root mean square error
SA	Sinoatrial
SMU	Single motor unit

Contents

Abbreviations and Acronyms	v
1 Introduction	1
2 Background	3
2.1 Physiology of ECG	3
2.1.1 Anatomy and function of the heart	3
2.1.2 Cardiac conduction system	5
2.2 Measurement of ECG	7
2.2.1 History and development of electrocardiography	7
2.2.2 Standard 12-lead ECG	8
2.2.3 Origin and morphology of the ECG signal	10
2.3 Baseline wander	13
2.4 Electromyogram	15
2.5 Inertial measurement units	16
2.6 Kalman filters	16
2.7 Baseline wander compensation with IMUs	18
3 Materials and methods	21
3.1 Data collection	21
3.2 Cross correlation of the IMUs	24
3.3 EMG signal processing	25
3.4 Adaptive Kalman filtering and smoothing	25
3.4.1 IMU attitude tracking	26
3.4.2 Electrode motion estimation	28
3.4.3 Motion artifact reduction	31
3.5 Butterworth high-pass filtering	32
3.6 Algorithm evaluation	33

4	Results	35
4.1	Collected data	35
4.2	EMG extraction	38
4.3	IMU cross correlations	40
4.4	Signal processing results	41
4.5	Algorithm performance evaluation	45
5	Discussion and conclusions	47
	References	51

Chapter 1

Introduction

Electrocardiography (ECG) (Webster, 2010) is a technique used to record the electrical activity of the heart. It is commonly used in medicine to monitor and diagnose patients with a cardiac condition. The advances in sensor and information technology have enabled ambulatory ECG recordings to be performed outside clinical settings in personal healthcare domain. These ambulatory ECG monitorings could lead to more representative data over longer time frames, thus improve the detection of arrhythmias and abnormal cardiac cycles that occur in paroxysmal manner or only under certain circumstances. For example, atrial fibrillation can be paroxysmal and stay easily undetected in the baseline ECG measurement (Higgins et al., 2013).

Atrial fibrillation is an independent risk factor for ischemic stroke that can even five-fold the risk without anticoagulation therapy (Wolf et al., 1991). Especially, patients who suffer from atrial fibrillation after a stroke have a high risk for a recurrent stroke. Currently, the clinical guidelines given by European Stroke Organisation (European Stroke Organisation (ESO), 2008) recommend 24-hour Holter monitoring after stroke. However, several studies (Gumbinger et al., 2012; Jabaudon et al., 2004; Higgins et al., 2013) have shown that paroxysmal atrial fibrillation detection can be improved with prolonged ECG monitoring (Grond et al., 2013). In addition to the improved detection, the ability to monitor the patients outside the hospital environment would make the recordings more comfortable for the patient and likely decrease the costs (Higgins et al., 2013).

Unfortunately, the ECG recordings performed during daily activities are prone to artifacts caused by body movements. One of these artifacts is low frequency baseline wander. The movement of the electrodes, with respect to the skin, changes the impedance on the electrode-skin interface, which causes the ECG baseline to wander (Webster, 2010). Artifact removal is crucial, since the artifacts complicate the clinical interpretation of the ECG

signal. Especially, when the longer recordings increase the amount of data and the automated classification of sections of interest is applied, the removal of artifacts becomes a requisite.

The non-computational denoising method of making the electrode-skin interface more stable is not powerful enough for removing the artifact from movement ECG measurements (Sörnmo and Laguna, 2005). Therefore, signal processing methods are needed. Classical high-pass filters are widely used, but they might remove also cardiac information or alter the signal morphology since the frequency spectra of the ECG signal and the baseline wander artifact are slightly overlapping (Sweeney et al., 2012). Adaptive filters, for example adaptive Kalman filters, have shown better performance in removing the artefact without distracting the cardiac signal (Hostettler et al., 2018). However, adaptive filters typically utilize a motion reference measured with additional sensors. For motion artifact, accelerometers are the most common reference sensors, although other sensors, such optical bend sensors, impedance sensors and skin stretch sensors have also been considered (Sweeney et al., 2012). The use of additional sensors cause the measurement device to be more complex, more expensive, and more energy-consuming.

The aim of this thesis is to develop an ECG signal baseline wander reduction method that does not rely on additional sensors. The artifact reduction in this thesis is scoped only to the baseline wander caused by motion. In terms of methods, this thesis is scoped to study only the feasibility of adaptive Kalman filters in baseline wander reduction. The proposed method uses electromyographic (EMG) signal as a motion reference signal for an adaptive Kalman filter algorithm. The reference EMG signal is obtained without any additional sensors by extracting it from the ECG signal with Butterworth high-pass filter. Another objective is to study if the number of sensors could be reduced in measurements that use accelerometer data as a reference signal for an adaptive Kalman filter.

This thesis is divided into five chapters. Chapter 2 provides a view on the background concepts: the principles of ECG, baseline wander artifact, electromyogram, inertial measurement units, and Kalman filters. Chapter 3 introduces the materials and methods used in the signal processing and algorithm evaluation. The results are presented in Chapter 4, and discussion and conclusions on the results are given in Chapter 5.

Chapter 2

Background

This chapter presents the physiological background of the ECG signal as well as the principles of measuring the ECG. Section 2.3 introduces the baseline wander artefact. Sections 2.4 and 2.5 provide descriptions of the EMG signal and the IMUs that are utilized in the Kalman filters. The proposed solutions for the artefact removal, Kalman filters, are introduced in Section 2.6 and their use with IMUs as a motion reference in Section 2.7.

2.1 Physiology of ECG

2.1.1 Anatomy and function of the heart

The heart functions as a pump for the cardiovascular system (Tortora and Derrickson, 2017). It has four chambers, two atria and two ventricles, whose cyclic contractions generate the blood flow. The atria receive blood from the veins which are blood vessels carrying blood toward the heart. The ventricles eject blood into vessels leaving the heart called arteries. Moreover, the heart is a double pump. The right part pumps blood into the pulmonary circulation, which takes care of the blood transfer to the lungs. Conversely, the left part runs the systemic circulation that delivers blood to the rest of the body. The ventricles are separated from the atria and the arteries by connective tissue valves to prevent the back flow of blood. The valves open and close in response to pressure changes caused by ventricle contractions and relaxations. The left and right ventricles are separated by a muscular wall called the interventricular septum. The structure of the human heart is illustrated in Figure 2.1.

Deoxygenated blood from the body enters the right atrium and is delivered to the right ventricle through the tricuspid valve (Tortora and Der-

rickson, 2017). The right ventricle contracts and pushes blood through the pulmonary valve into an artery called the pulmonary trunk that carries blood to the lungs. The excess carbon dioxide is released and new oxygen picked up in thin vessels called the pulmonary capillaries. The oxygenated blood flows back to the heart through the pulmonary veins and enters the left atrium. Blood is transferred to the left ventricle through the bicuspid valve. The contraction of the heart pushes blood through the aortic valve into the aorta from which it is distributed throughout the body via systemic arteries. The exchange of the gases as well as nutrients takes place in systemic capillaries. After the exchange, deoxygenated blood flows back to the right atrium of the heart via systemic veins.

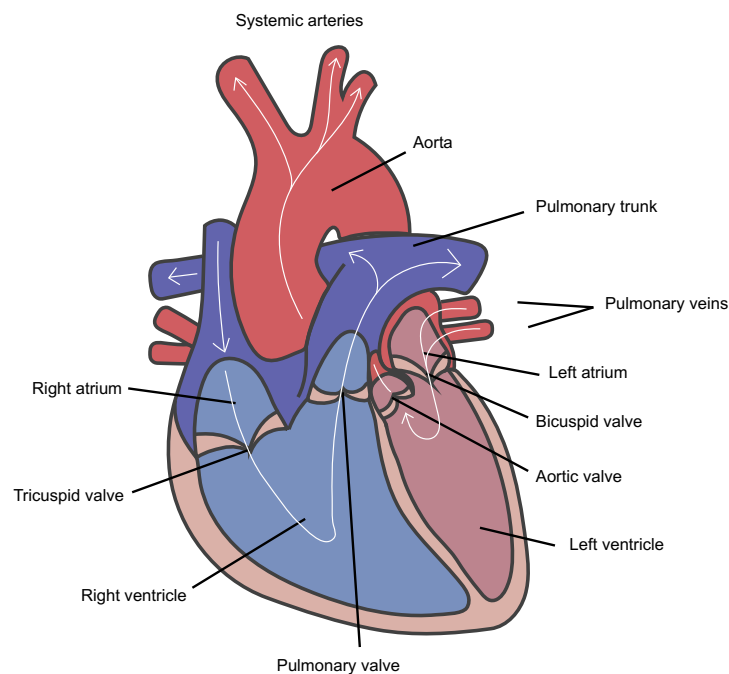


Figure 2.1: The human heart is divided into two halves which both contain an atria and a ventricle. Deoxygenated blood enters the right atrium and continues to the pulmonary trunk via the right ventricle. Blood is oxygenated in the lungs and then returns to the heart via pulmonary veins. Oxygenated blood flows from the left atrium to the left ventricle before being delivered throughout the body via the aorta. The blood flow inside the heart is restricted by valves that only open during contractions. Blood vessels carrying oxygenated blood are colored red and blood vessels carrying deoxygenated blood are colored blue. Direction of the blood flow is marked with arrows.

2.1.2 Cardiac conduction system

The heart wall is made of three layers: the external connective tissue layer called the epicardium, the middle layer called the myocardium and the inner endothelium layer called the endocardium (Tortora and Derrickson, 2017). The myocardium covers 95% of the heart wall. It is composed of cardiac muscle tissue and is responsible for the contractions and relaxations of the heart.

Cardiac muscle fibers are striated, cylindrical fibers that may be divided into branches. The connections between the adjacent fibers are specialized membranes called intercalated discs (Strootbandt et al., 2016). Since the intercalated discs contain gap junctions with very low electrical resistance, they allow a rapid conduction of action potentials from one cell to another. As a result, the heart muscles function as a synchronous unit. In addition, cardiac muscle cells have a semipermeable cell membrane with selective ion channels. Those channels let only specific charged particles to pass through the membrane either into the cell or out of it. The selectivity of the membrane creates a potential difference between the sides of the membrane, referred to as resting membrane potential. In cardiac muscle fibers the resting membrane potential is close to -90 mV (Tortora and Derrickson, 2017).

About 1% of the muscle fibers are autorhythmic fibers that have the ability to excite action potentials in themselves (Tortora and Derrickson, 2017). The autorhythmic fibers have two important functions. Firstly, they act as a pacemaker and thus pace the contractions of the heart by controlling the action potential excitations. Secondly, they form the cardiac conduction system. The conduction system is a network of autorhythmic fibers that works as a pathway for the cardiac excitations to proceed throughout the heart. The rest of the muscle fibers are contractile fibers that contract when they receive the action potential from the conduction system (Tortora and Derrickson, 2017).

Electrical activation of the heart begins from the sinoatrial (SA) node in the right atrium (Tortora and Derrickson, 2017). The SA-node cells depolarize spontaneously and repeatedly to the threshold potential that triggers the action potential. The action potential travels through both atria via gap junctions and generates the simultaneous contraction of the atria that pushes blood to the ventricles. The propagation of the action potential is slowed down in the atrioventricular (AV) node to give time for the atria to drain. Next, the action potential proceeds to the ventricles via the atrioventricular bundle which is the only electrically conductive pathway between the atria and the ventricles. The bundle diverges into left and right branches which carry the signal to the apex of the heart. From there, the action potential

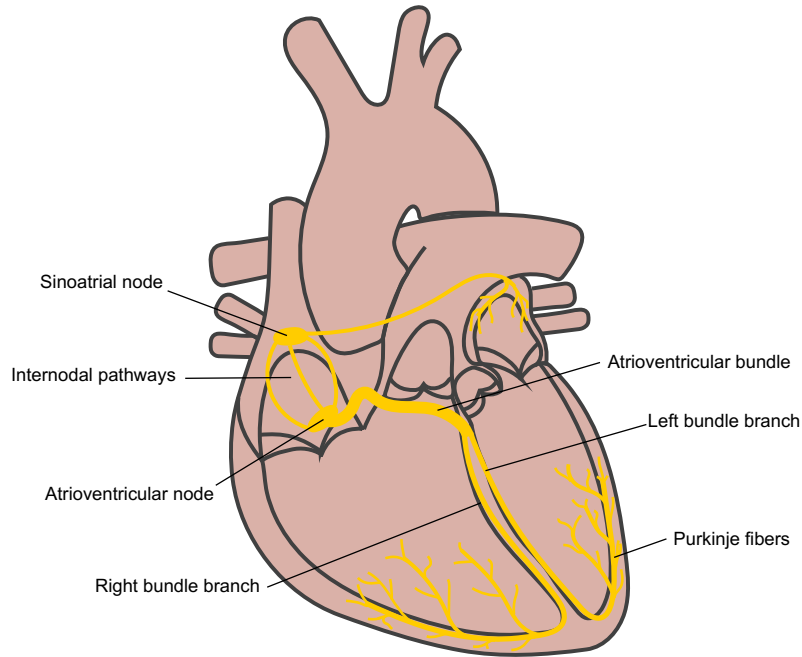


Figure 2.2: Electrical activation of the human heart begins with the sinoatrial node depolarization. The action potential propagates through both atria causing them to contract. The propagation is slowed down in the atrioventricular node to give time for the atria to drain. Next, the action potential continues to proceed via the atrioventricular bundle and the bundle branches to the Purkinje fibers that generate the contraction of the ventricles. The conduction pathways are colored yellow.

spreads rapidly upward the ventricles via Purkinje fibers. The spreading action potential causes the sequential contraction of the contractile fibers. The ventricles contract and push the blood toward the semilunar valves. The conduction system of the heart is visualized in Figure 2.2.

The SA-node initiates action potentials in a constant rate of about 100 times per minute (Tortora and Derrickson, 2017). However, the amount of blood supply needed in the tissues is not constant but varies under different conditions. The body adapts to the changing needs by regulating the heart rate. The most important regulation mechanisms is the autonomic regulation. The autonomic regulation originates in the cardiovascular center in the brainstem (Tortora and Derrickson, 2017). If the need for the blood increases in the tissues, for example, during physical activity, the cardiovas-

cular center increases the frequency of nerve impulses in the sympathetic nerves. Impulses in the sympathetic cardiac accelerator nerves trigger the release of norepinephrine that raises the rate of the spontaneous depolarization in the SA-node. Conversely, if the heart rate needs to be decreased, for example, during rest or sleep, the cardiovascular center increases the impulse frequency in the parasympathetic nerves. The parasympathetic vagus nerves release acetylcholine to the vicinity of the SA-node, AV-node, and atrial myocardium, which decreases the rate of the spontaneous depolarization in their autorhythmic fibers. With the autonomic nerve stimulations, the heart rate can be controlled to vary from 20–30 beats/min up to over 200 beats/min (Tortora and Derrickson, 2017). In addition to the autonomic regulation, several chemicals, like hormones and cations, affect the heart rate. Furthermore, factors like age, gender, physical condition, and body temperature all affect the resting heart rate and the possible maximum heart rate of an individual.

2.2 Measurement of ECG

2.2.1 History and development of electrocardiography

Electrocardiography (ECG) is a technique to record the electrical activity of the heart. The first observations of bioelectrical activity were made in 1786 by Luigi Galvani (AlGhatrif and Lindsay, 2012). Galvani managed to record electrical current from dissected animal skeletal muscles. In 1842, Carlo Matteucci proved with frogs that also heart beats are associated with electrical current (AlGhatrif and Lindsay, 2012).

The first human ECG was recorded in 1887 by Augustus D. Waller (Waller, 1887). It was recorded with capillary electrometer and surface electrodes attached to the chest and back. Waller also proved that the electrical activity preceded the ventricular contractions by recording the ECG and the movements of the heart simultaneously. In 1901, Willem Einthoven succeeded to develop a new string galvanometer for more sensitive recordings (Barold, 2003). Furthermore, Einthoven discovered the PQRST-waveform of the ECG signal and the three standard limb leads (I, II and III) of ECG recordings known as Einthoven’s triangle. Later, he was awarded the Nobel Prize for discovering the mechanism of ECG.

Over the first decades of the 20th century, the clinical usage of the three-lead ECG extended especially after improving the portability. Initially, the ECG was used mainly to study arrhythmias. The diagnostic significance increased after discovering that also myocardial infarctions could be diagnosed

with ECG. The study of myocardial pathology led to the development of new leads. The six unipolar chest leads (V1-V6) were standardized in 1938 (AlGhatrif and Lindsay, 2012). Finally, the augmented unipolar limb leads (a-VL, a-VR and a-VF) were established leading to the standardization of 12-lead ECG in 1954 (AlGhatrif and Lindsay, 2012).

Currently, ECG is routinely used in medical diagnostics and there is a range of ECG devices available. In addition to the standard 12-lead ECG, there are for example ambulatory Holter monitors and multichannel body surface mapping systems (Trobe et al., 2018). Additionally, wearable and wireless ECG devices are emerging as a method for continuous monitoring in elderly people healthcare (Baig et al., 2013) as well as in consumer products with mobile applications.

2.2.2 Standard 12-lead ECG

The standard 12-lead ECG consists of three bipolar limb leads, three augmented limb leads, and six unipolar precordial leads (Trobe et al., 2018). The limb leads record in the frontal plane of the body and the precordial leads in the transverse plane. The term bipolar lead is used to describe that the leads reflect the voltage difference between a pair of electrodes, whereas the term unipolar lead refers to the voltage variations of a single electrode in relation to a reference electrode (Sörnmo and Laguna, 2005). The bipolar limb leads are recorded with electrodes placed on the left arm (LA), right arm (RA), and left leg (LL). Typically, one electrode is placed on the right leg (RL) to serve as an reference electrode. Lead I measures the potential difference between LA and RA, lead II between LL and RA, and lead III between LL and LA. The resulting lead vectors can be approximated to form the Einthoven's triangle, an equilateral triangle with the electrodes as its corners and the heart as its center (Webster, 2010). As a result, the leads I, II, and III are noted to reflect the potential differences in the frontal plane in the directions with 0° , 60° and 120° angles, respectively.

To cover more directions in the frontal plane, the augmented limb leads aVF, aVL, and aVR were introduced (Sörnmo and Laguna, 2005). They are unipolar leads having a reference electrode called the Wilson central terminal (Wilson et al., 1934). The Wilson central terminal is formed by connecting the three limb electrodes through equal-valued resistances to a central terminal. The voltage at the central terminal is the average of the voltages at the limb electrodes. The lead from the Wilson central terminal (V) to LA is known as VL, to RA as VR and to LL as VF. However, for each lead, one of the resistances shunts the circuit between the electrode and the central terminal, which leads to very small amplitude (Webster, 2010).

To increase the amplitude, the limb being measured and the central terminal are disconnected, thus the augmented limb leads are formed. The augmented leads, known as aVL, aVR and aVF, correspond to the directions with -30° , -150° and 90° angles, respectively. The lead angles in the frontal plane are shown in Figure 2.3.

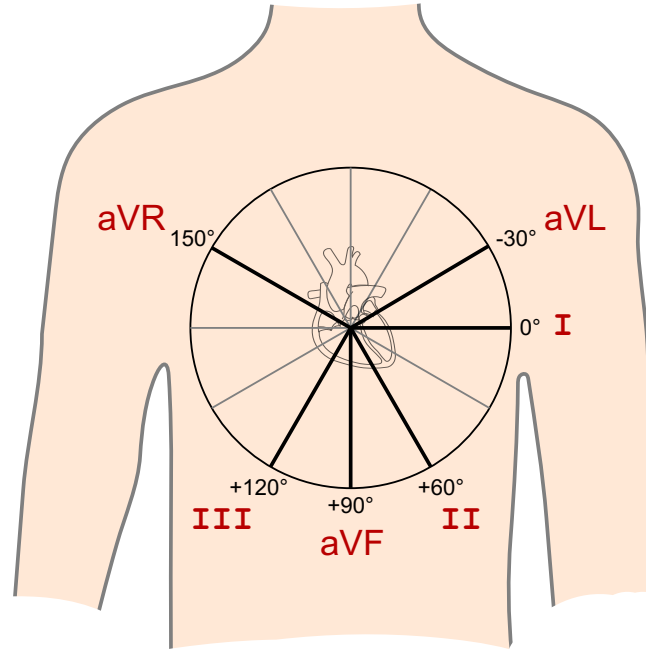


Figure 2.3: The lead angles of the limb leads and augmented limb leads. The limb leads and augmented limb leads reflect the potential differences in the frontal plane with angles of 0° , 60° , 90° , 120° , -30° and -150° relative to the heart.

In order to get a view of the heart in the transverse plane, six precordial leads are measured in the standard 12-lead ECG. Six chest electrodes are placed in anatomically defined positions on the front and left side of the chest wall. The potential differences are measured between the chest electrodes and the Wilson central terminal. The resulting leads, named from V1 to V6, cover the transverse plane directions from 0° to 100° with steps of 20° angle (Trobec et al., 2018). The placement of both limb and precordial electrodes is shown in Figure 2.4.

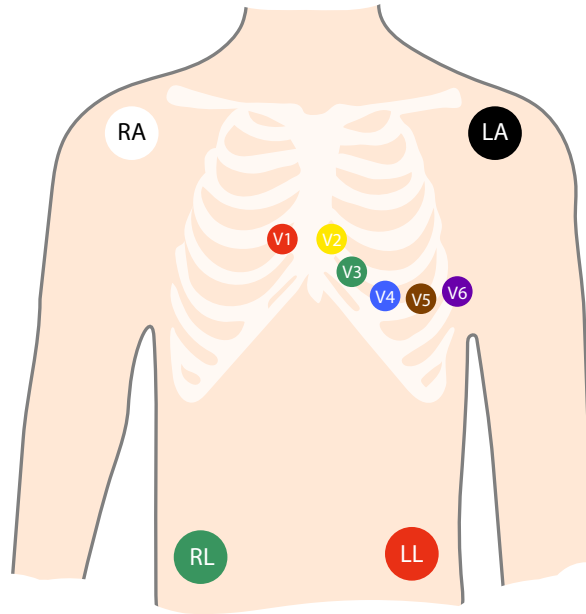


Figure 2.4: The placement of the electrodes in the standard 12-lead ECG. The recording limb electrodes are placed on the right arm, left arm, and left leg. The reference electrode is placed on the right leg. The precordial electrodes are placed on the front and left side of the chest wall.

2.2.3 Origin and morphology of the ECG signal

As described in Section 2.1.2, the action potential generated in the SA node proceeds along the conduction system and excites the contractile muscle fibers. In the contractile fibers, the action potential occurs in three stages: first the fiber depolarizes, next comes the plateau and eventually the fiber repolarizes back to the resting state (Tortora and Derrickson, 2017). The depolarization begins when the additive action potentials from the neighbouring fibers bring the membrane potential of the fiber to the threshold potential. Reaching the threshold potential causes the opening of the sodium ion channels of the membrane. Positively charged sodium ions flow into the negatively charged muscle fiber cytosol down the electrochemical gradient. The ion inflow produces a rapid depolarization of the fiber, which again closes the sodium ion channels. During the next phase, plateau, the depolarization is maintained by the balanced inflow of positive calcium ions and outflow of positive potassium ions down the concentration gradients. Finally, the repolarization restores the membrane potential to its negative resting value.

The repolarization is achieved by closing the calcium ion channels and opening additive potassium ion channels for increased potassium ion outflow. A figure of the phases in myocardial action potential is shown in Figure 2.5.

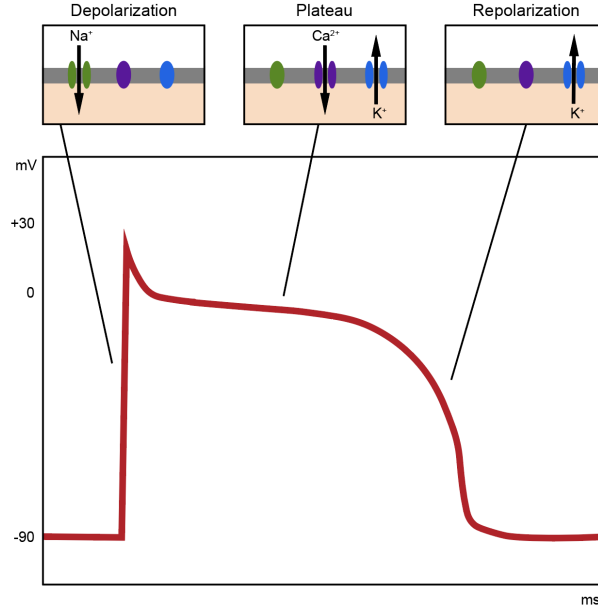


Figure 2.5: Myocardial action potential is divided into three stages: depolarization, plateau and repolarization. The depolarization is achieved by the inflow of positive sodium ions. During the plateau, the depolarization is maintained by balanced inflow of positive calcium ions and outflow of positive potassium ions. The repolarization restores the negative resting value by positive potassium ion outflow.

An electrocardiogram is a recording of the combined action potentials produced by all of the heart muscle fibers (Tortora and Derrickson, 2017). The depolarization and repolarization waves during each heartbeat produce voltage changes that form the typical PQRST-waveform of the ECG recordings. The ECG signal morphology is dependent on the ECG measurement angles, which in turn are dependent on the leads, both presented in Section 2.2.2. A typical ECG signal measured from lead I is shown in Figure 2.6.

The electrical activation in the SA-node is too weak to be recorded at the body surface, thus the first visible deflection in the ECG recording is caused by the next event, the atrial depolarization (Katz, 2011). The atrial depolarization produces the P-wave, which is followed by the QRS complex representing the ventricular depolarization. The third deflection is the T-wave,

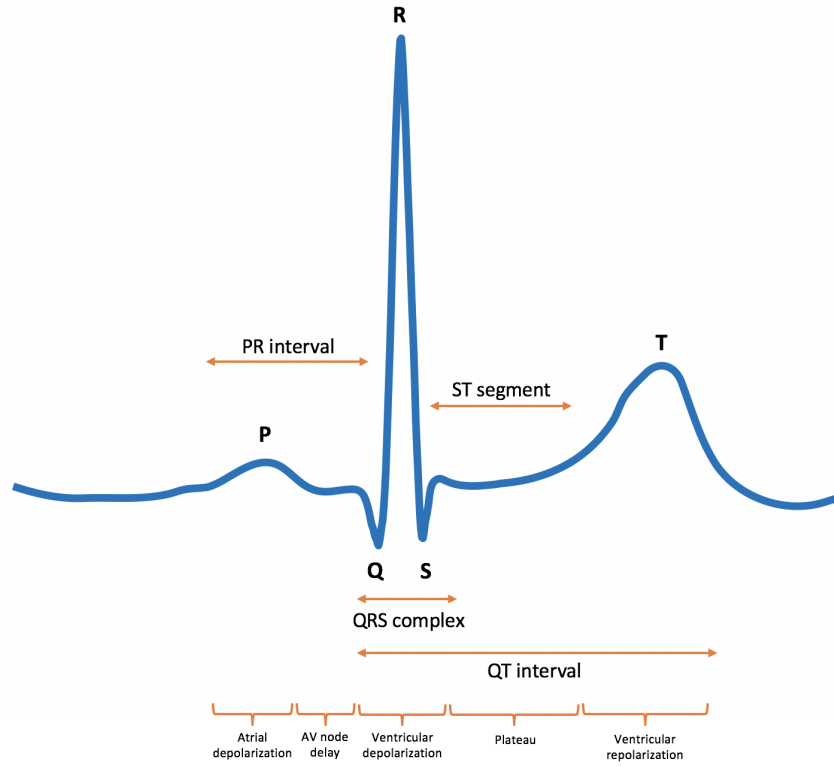


Figure 2.6: ECG signal morphology over one cardiac cycle. The P-wave is produced by the atrial depolarization, the QRS complex by the ventricular depolarization, and the T-wave by the ventricular repolarization. The P-R interval describes the action potential conduction time, the Q-T interval the duration of the ventricular action potential, and the S-T segment the duration of the plateau.

which corresponds to the repolarization of the ventricles. Between these deflections, the ECG normally returns to its baseline. In ECG analysis, the amplitudes and shapes of the waves are examined to identify abnormalities in heart function.

In addition to the waves, also the time spans between the waves provide important information of the function of the heart (Tortora and Derrickson, 2017). The length of the interval between the atrial and ventricular activation, called the P-R interval, describes the action potential conduction time through the AV-node, AV-bundle, bundle branches, and the Purkinje fibers (Katz, 2011). The Q-T interval represents the total duration of the ventricular action potential, and the S-T segment the duration of the plateau phase

only.

The frequency spectrum of a normal ECG signal in sinus rhythm has distinct characteristics. The accepted frequency range for diagnostic ECG is 0.05–100 Hz (Orphanidou, 2018). Although, the power of a typical QRS complex is in the frequencies below 30 Hz. The peak power occurs in the range of 4–12 Hz, including the QRS complex as well as the P- and T-waves. (Murthy et al., 1978). Normally, the highest peak, R-peak, has an amplitude of maximum 3 mV (Sörnmo and Laguna, 2005).

2.3 Baseline wander

The diagnostic quality of ECG measurements can be affected by various types of disturbances. The presence of the artifacts as well as poor processing of the signal can lead to incorrect diagnoses when interpreting the ECG. The disturbances are typically electrical interferences and can be categorised into physiological and non-physiological artifacts (Crawford and Doherty, 2011). The physiological artifacts include the movement artifacts baseline wander and electromyographic noise. The non-physiological artifacts can be caused for example by power lines, ground loops, loose electrode-lead connections, or electrode misplacements. In this section, the movement artifact baseline wander is presented.

The wandering of the ECG baseline is a motion artifact caused by impedance changes at the electrode-skin interface. In an ideal measurement, the ECG signal would be constantly centered at zero from where the waves would deviate. In baseline wander, the center of the waves shifts from zero in slow fluctuations. Figure 2.7 shows an example of an ECG signal with significant baseline wander. There are two main methods how the baseline wander can be induced (Webster, 2010). Firstly, if the electrode moves with respect to the skin, the movement disturbs the charge distribution either at the electrode-electrolyte or the electrolyte-skin interface. Secondly, stretching the skin or applying pressure to it, may change the skin potential several millivolts.

Especially in the ECG measurements performed during motion, the baseline wander is often accompanied with an electromyographic artifact. Typical causes for baseline wander are body movements, poor electrode contact, movement of cables, respiration, and perspiration. The spectral content of the baseline wander artifact is typically less than 1 Hz, but doing physical exercises during the recording may add higher frequency components (Sörnmo and Laguna, 2005). The magnitude of the artifact can be several times higher than the amplitude of the QRS complex.

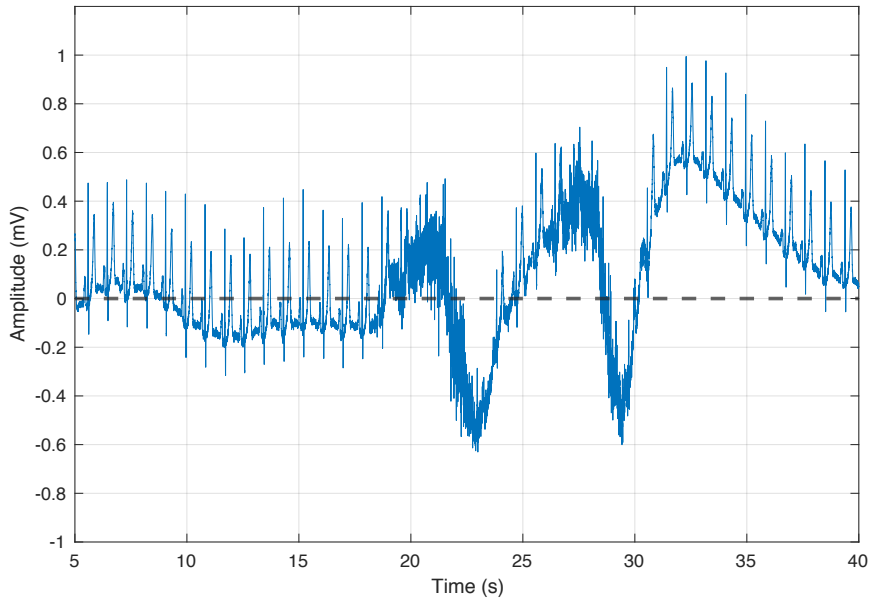


Figure 2.7: ECG signal with wandering baseline. The baseline wander is a motion artifact caused by impedance changes at the electrode-skin interface. The baseline wander appears as a slow fluctuation of the ECG baseline from the zero-line that is marked with dashed line. There is also electromyographic noise visible from $t \approx 19$ s to $t \approx 31$ s.

The amount and intensity of the motion artifacts increase when shifting from clinical resting ECG recordings into longer ambulatory measurements. The baseline wander can be reduced by improving the stability of the electrode-skin interface. This can be achieved by using nonpolarizable electrodes, removing the stratum corneum layer of the skin, or using microneedle electrodes that pass through the stratum corneum and the barrier layer of the skin (Webster, 2010). However, these methods can not completely prevent the occurrence of baseline wander and some of them can be painful for the patient. Therefore, signal processing methods are needed. Two major computational techniques used to remove the baseline wander are linear filtering and polynomial fitting (Sörnmo and Laguna, 2005). Yet, despite their wide use and rather easy implementation, these classical filtering techniques have some major drawbacks. Since the spectral contents of the ECG signal and the baseline wander artifact are typically slightly overlapping, for example, high-pass filtering might also remove some important cardiac information (Sweeney et al., 2012). Moreover, if the phase response of the filter is not linear, it might also alter the ECG morphology (Kaur and Singh, 2011).

2.4 Electromyogram

Like Section 2.3 presented, the electromyographic signal in ECG is usually considered as an artifact. However, electromyogram (EMG) also gives valuable information of muscle activity that is often related to movement. In this thesis, the electromyographic interference in ECG is utilized as a reference signal for the Kalman filter, indicating patient movement during the recording.

The EMG signal originates from the electrical activity of the skeletal muscles (Sörnmo and Laguna, 2005). The skeletal muscles are involved in producing movement as well as in maintaining the body position. The skeletal muscles are organized in motor units, which include a single motor nerve fiber and the muscle fibers to which it is attached (Webster, 2010). A single motor unit (SMU) represents the smallest functional unit of volitional contraction. As in the cardiac muscle tissue, also the skeletal muscle fiber contractions are controlled by the action potentials. The SMU contracts when the action potential coming from the innervating motor neuron spreads along the excitable membranes of the muscle fibers. Thus, the active muscle fibers of the SMU constitute a bioelectric source (Webster, 2010), which evokes field potentials that can be recorded from body surface. The EMG signal is a summation of the motor unit action potentials that are sufficiently close to the recording electrode. The amplitude of the surface EMG signal is typically in the range of 0.25–5 mV (Sörnmo and Laguna, 2005). The frequency range is wide and partially overlapping with the spectral content of ECG signal.

Since the ECG electrodes are measuring heart induced potentials from the body surface, they also capture the EMG signal from the superficial muscles near them. Especially, when the ECG is recorded during exercise, a significant amount of muscular activation occurs which results in EMG contaminated ECG signal. In this thesis, the ECG is recorded while the subjects are performing certain motion sequences. Thus, the ECG signal features also EMG components. The aim is to use an adaptive Kalman filter to reduce the amount of motion related baseline wander in the ECG signal. Since the baseline wander and the EMG signal are both motion artifacts, they can be assumed to originate from the same motion. Therefore, the extracted EMG signal is used as a reference signal providing information on the amount of the measurement noise for the Kalman filter. The principles of Kalman filters are introduced in Section 2.6 and the more detailed description of the reference signal usage for modeling motion is given in Section 3.4.

2.5 Inertial measurement units

An inertial measurement unit (IMU) is an electronic device that measures the position changes of the measured object (Kempe, 2011). The modern IMUs typically consist of accelerometer, gyroscope and magnetometer (Ahmad et al., 2013). Commonly, they are all tri-axial, gaining together nine degrees of freedom (DOF). The accelerometer is used to measure the inertial acceleration whereas the gyroscope measures the angular rotation. The magnetometer measures the yaw angle rotation from magnetic fields and is used to improve the reading of the gyroscope that is easily disturbed by drift. IMUs are commonly used in applications of navigation systems, robotics, and industry quality control. In medical applications, they can be used, for example, in long term health monitoring (Rodríguez-Martín et al., 2013) and in pose estimation (Tobergte et al., 2009).

In this thesis, and in adaptive ECG signal denoising in general, IMUs are used to measure the movement of the electrodes. The electrode movement is then used as a reference signal for an adaptive filter that removes the motion artifact. The adaptive Kalman filter algorithm presented by Hostettler et al. (2018), and used in this thesis, utilizes the data from all three sensors when estimating the motion of the electrode. The algorithms and the use of reference signals are presented in Section 3.4. Although the use of IMUs as a motion reference is an effective method in motion artifact reduction, this thesis studies, if a successful artifact removal could be achieved with a reduced number of IMUs or even without any additional sensors.

2.6 Kalman filters

Kalman filter (Kalman, 1960) is an recursive estimator used to estimate the states of a linear Gaussian dynamic system. The Kalman filter utilizes the measurement data as well as prior knowledge about the measurement device and the system to provide an optimal system state estimate with statistically minimised error (Mason, 2002). The Kalman filter consists of two steps, prediction step and update step (Welch and Bishop, 1995). In the prediction step, the filter produces an *a priori* estimate of the system state in the next time step based on the previous estimate. Next, the new measurement is used to refine the *a priori* estimate to obtain an improved *a posteriori* estimate. After each prediction and update step pair, the Kalman filter loop is repeated. The previous *a posteriori* estimates are used to predict the next *a priori* estimates, hence the recursive nature. The function of the Kalman filter is based on the assumption that the dynamic system is linear and the

noise is Gaussian. However, there are variations available for nonlinear and non-Gaussian problems, such as the extended Kalman filter (Sweeney et al., 2012).

Kalman filtering is computationally efficient due to its matrix operations. In addition, the recursive nature makes the real-time implementations of Kalman filter feasible. Consequently, the Kalman filter has found many applications, to a great extent in the fields of navigation and target tracking. The number of applications in biomedical signal processing is smaller but increasing. For example, adaptive Kalman filters have been proposed as a method for ECG baseline wander removal, for example, by Hostettler et al. (2018) and Mneimneh et al. (2006). Further, Vullings et al. (2010) successfully used adaptive Kalman filter and Sameni et al. (2005) and Sayadi and Shamsollahi (2008) extended Kalman filter for ECG signal denoising, but targeting the high frequency noise instead of the baseline wander.

The Kalman filter state-space model (Equation 2.1) describes a system where the evolution of the system state \mathbf{x}_k follows a linear dynamic model with Gaussian process noise and the measurements \mathbf{y}_k are linearly related to the system state with Gaussian noise (Kovvali et al., 2014). The dynamic model and measurement model are given as (Särkkä, 2013; Welch and Bishop, 1995):

$$\mathbf{x}_k = \mathbf{A}_{k-1}\mathbf{x}_{k-1} + \mathbf{q}_{k-1}, \quad (2.1a)$$

$$\mathbf{y}_k = \mathbf{H}_k\mathbf{x}_k + \mathbf{r}_k, \quad (2.1b)$$

where $\mathbf{x}_k \in \mathbb{R}^n$ is the state of the system at time step k and $\mathbf{y}_k \in \mathbb{R}^m$ is the measurement at time step k . The state transition matrix of the dynamic model \mathbf{A}_{k-1} relates the state at the previous time step $k-1$ to the current state. The measurement model matrix \mathbf{H}_k gives the connection between the state \mathbf{x}_k and the measurement \mathbf{y}_k . The random variables \mathbf{q}_k and \mathbf{r}_k denote the process noise and measurement noise, respectively. They are assumed to be independent and white with normal probability distributions $\mathbf{q}_k \sim \mathcal{N}(\mathbf{0}, \mathbf{Q}_{k-1})$ and $\mathbf{r}_k \sim \mathcal{N}(\mathbf{0}, \mathbf{R}_k)$. The process noise covariances \mathbf{Q}_{k-1} and the measurement noise covariances \mathbf{R}_k are assumed to be given.

In the prediction step, the *a priori* system state estimate \mathbf{m}_k^- and its covariance matrix \mathbf{P}_k^- are calculated using the *a posteriori* estimates of the previous time step (for in-depth derivations of the Kalman filter equations, refer to, for example, Särkkä (2013)) :

$$\mathbf{m}_k^- = \mathbf{A}_{k-1}\mathbf{m}_{k-1}, \quad (2.2a)$$

$$\mathbf{P}_k^- = \mathbf{A}_{k-1}\mathbf{P}_{k-1}\mathbf{A}_{k-1}^\top + \mathbf{Q}_{k-1}. \quad (2.2b)$$

The predicted system state estimate is used in the update step to obtain the predicted measurement estimate \mathbf{z}_k :

$$\mathbf{z}_k = \mathbf{H}_k \mathbf{m}_k^- . \quad (2.3)$$

Next, the error in the estimated measurement \mathbf{v}_k , the *innovation*, can be calculated with the actual measurement value \mathbf{y}_k :

$$\mathbf{v}_k = \mathbf{y}_k - \mathbf{z}_k . \quad (2.4)$$

The covariance matrix of the prediction error is named as innovation matrix and can be calculated as:

$$\mathbf{S}_k = \mathbf{H}_k \mathbf{P}_k^- \mathbf{H}_k^\top + \mathbf{R}_k . \quad (2.5)$$

The weighting matrix, Kalman filter gain, that minimizes the *a posteriori* estimation error covariance can be calculated as:

$$\mathbf{K}_k = \mathbf{P}_k^- \mathbf{H}_k^\top \mathbf{S}_k^{-1} . \quad (2.6)$$

Finally, the *a posteriori* state estimate \mathbf{m}_k and its covariance matrix \mathbf{P}_k are updated:

$$\mathbf{m}_k = \mathbf{m}_k^- + \mathbf{K}_k \mathbf{v}_k , \quad (2.7a)$$

$$\mathbf{P}_k = \mathbf{P}_k^- - \mathbf{K}_k \mathbf{S}_k \mathbf{K}_k^\top . \quad (2.7b)$$

2.7 Baseline wander compensation with IMUs

This thesis is a continuation of the study by Hostettler et al. (2018) which represents the state of the art in ECG baseline wander reduction. Hostettler et al. (2018) proposed a baseline wander compensation algorithm that is based on adaptive Kalman filtering and IMUs. They attached the IMUs to each recording electrode and recorded ECG while the subjects performed motions. The IMUs were used to estimate the local electrode motion which served as a reference signal for the Kalman filter.

The local electrode motion was estimated with the Kalman filtering and smoothing algorithm for attitude tracking introduced by Särkkä et al. (2015). The attitude tracker estimates the attitude of each IMUs by tracking the gravity and magnetic field vectors in the local coordinate frames of the IMUs. The estimated attitudes were used to estimate the relative motions of the IMUs in global coordinates. The motion estimation was performed again with a Kalman filter using an inertial navigation model (Titterton and Weston,

2004) as the dynamic model and the attitudes as inputs. Finally, the motion artifact reduction was done with a Kalman filter using the estimated local positions as a reference signal and modeling the ECG measurement as a superposition of the cardiac signal and the baseline wander disturbance. The result was the estimate of the motion artifact reduced ECG signal. Section 3.4 presents the above mentioned adaptive Kalman filtering and smoothing algorithm in detail.

Hostettler et al. (2018) evaluated the algorithm by performing clinical trials. In the trials, the ECG and the IMU data were simultaneously recorded from 20 subjects that were performing sequences of motions. The motion artifact reduction algorithm was applied to that clinical trial data. With this approach, they managed to remove the baseline wander artifact without significantly changing the ECG signal morphology. Figure 2.8 shows the motion compensated ECG signal in comparison with the raw signal. The baseline wander has been mostly removed. Figures 2.9 and 2.10 show the morphology comparison of the compensated and raw ECG signal in periods of no motion and motion, respectively. The processed signals are slightly altered, but the morphology has stayed mostly intact.

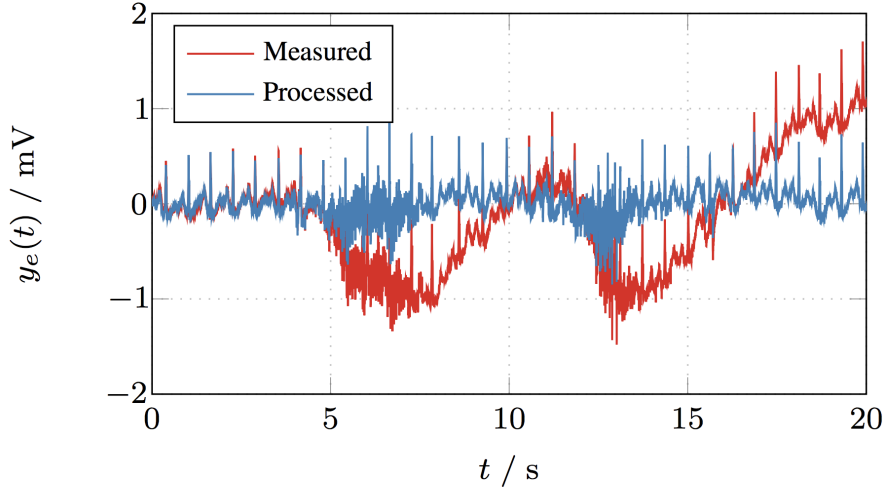


Figure 2.8: Example of the raw and baseline wander compensated lead II ECG signals. The baseline wander compensation algorithm using IMU data as a motion reference for Kalman filter has successfully removed most of the baseline wander. (Hostettler et al., 2018)

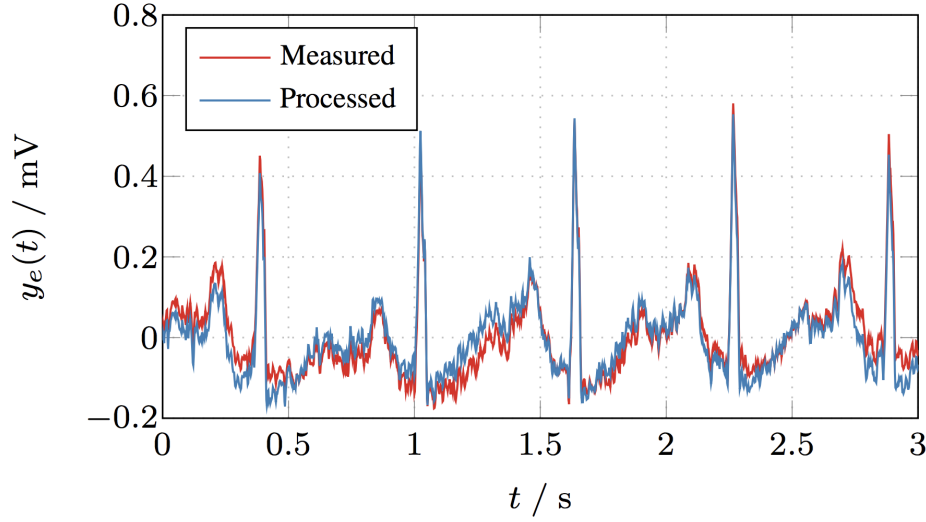


Figure 2.9: Comparison of the measured and processed ECG during a period without motion artifacts. The processing has not significantly altered the ECG signal morphology. (Hostettler et al., 2018)

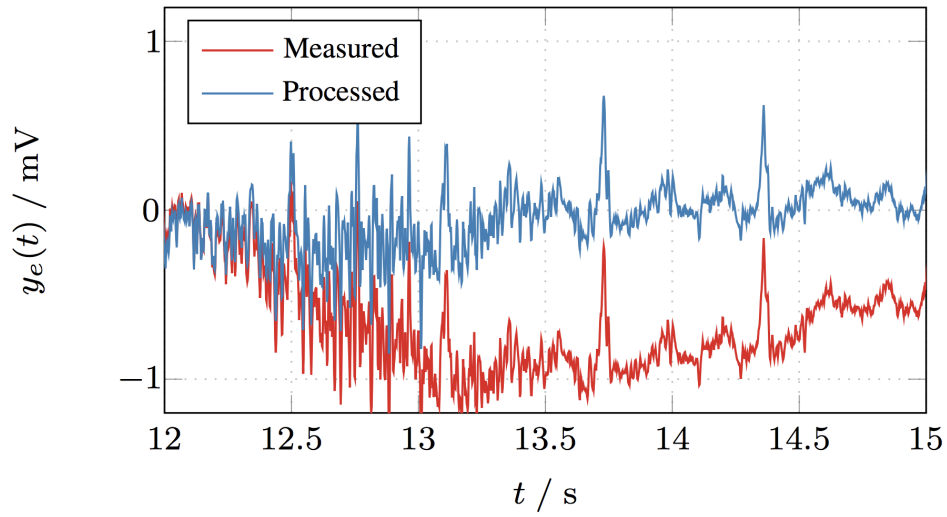


Figure 2.10: Comparison of the measured and processed ECG during a period with motion artifacts. The processing has not significantly altered the ECG signal morphology. (Hostettler et al., 2018)

Chapter 3

Materials and methods

This chapter describes the data collection and the methods used in the study. All signal processing was implemented in MATLAB R2019b.

3.1 Data collection

In this thesis, the same combined ECG and IMU measurement data was used that was recorded by Hostettler et al. (2018). The clinical trials were approved by the Ethics Committee of the Helsinki and Uusimaa Hospital District.

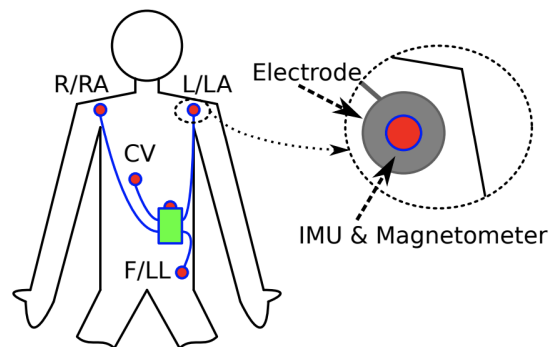


Figure 3.1: Illustration of the experimental setup. Three-lead ECG setup is used with four electrodes placed as marked with red dots and one reference electrode attached to the ECG device marked with green box. A wireless motion sensor including an IMU and a magnetometer is attached on top of each electrode. (Hostettler et al., 2018)

The ECG was measured with a three-lead ambulatory ECG device (Faros 360, Bittium Biosignals, Oulu, Finland). The device contains five electrodes forming the lead I from R/RA to L/LA, lead II from R/RA to F/LL, and lead V1 from CV to F/LL with the reference electrode, Faros, integrated in the device. The electrodes used were Ag/AgCl electrodes with wet gel. Additionally, a motion sensor was attached on top of each electrode. The motion sensors (MetaMotion C, mBientlab, San Francisco, CA) included an inertial measurement unit (BMI160, Bosch Sensortec, Reutlingen, Germany) and a magnetometer (BMM150, Bosch Sensortec, Reutlingen, Germany). The electrode placements are shown in Figure 3.1, the ECG device used in Figure 3.2, and the motion sensors in Figure 3.3.



Figure 3.2: The three-lead ambulatory ECG device (Faros 360, Bittium Biosignals) used in the data collection. Photo by Simo Särkkä.

The ECG signals were sampled at 1000 Hz, the accelerometers and the gyroscopes were sampled at 100 Hz, and the magnetometers were sampled at 25 Hz. The clocks of the ECG device and the motion sensors were synchronized by performing a heel drop motion and estimating the delay by calculating the cross correlation of the Faros accelerometer and the integrated accelerometer in the ECG device.

The clinical trials were performed with 20 subjects, from which 10 were healthy and 10 had a cardiac condition. The subjects were asked to perform a set of seven motion sequences that simulate common everyday activities. Each motion sequence was performed twice. The motion sequences were:



Figure 3.3: The motion sensors (MetaMotion C, mBientlab) used in the data collection. The motion sensors consist of an inertial measurement unit and a magnetometer. Photo by Simo Särkkä

1. Patient is lying on their back. Patient rolls on right side 90 degrees then returns to backside position.
2. Patient stands up from sitting position.
3. Patient is standing with upper limbs extended, then reaches floor without bending their knees.
4. Patient is starting with upper limbs rotated outwards and elbow joints at 90 degrees flexed. Keeping elbows flexed patient moves forearms together to the front.
5. Patient starts with upper limbs resting on sides, elbow joints extended. Keeping elbows extended, patient raises upper limbs above head forming a 180 degrees angle.
6. Patient starts with elbows flexed at 90 degrees, forearms touching in front, patient rotates upper body laterally on right side, returns to front, then left side, and returns to front.
7. Patient walks in staircase, arms freely moving.

3.2 Cross correlation of the IMUs

For modeling the motion artifact component of the Kalman filter, Hostettler et al. (2018) used the data from the IMUs attached to those two electrodes that were recording a certain ECG lead. Their method requires as many IMUs as there are electrodes measuring ECG. In this thesis, a cross correlation check was performed across all of the IMUs to see if the number of IMUs could be reduced over redundancy in the data. Pyysing (2018) has previously studied the correlation between the ECG signal during motions and acceleration. The data set was small, but her results suggested that the correlation would be more dependent on the type of the motion than on the accelerometer location. Therefore, it might be possible that the accelerations from different locations would correlate with each other so significantly that the number of them could be reduced.

Cross correlation describes the similarity of two series as a function of the shift relative to the other. The cross correlation of two jointly stationary random zero mean processes x_n and y_n is given by

$$R_{xy}(m) = E\{x_{n+m}y_n^*\}, \quad (3.1)$$

where E is the expected value operator, the asterisk denotes complex conjugation, and $-\infty < n < \infty$.

In the cross-correlation check, only the z -axis accelerations were under examination since they were thought to contain the most relevant information about the motions. The cross correlation values were calculated with Matlab's normalized *xcorr* function using the maximum of 200 samples (0.2 seconds) lag. The normalization in the Matlab's cross correlation function normalizes the sequence so that the autocorrelations at zero lag equal 1:

$$\hat{R}_{xy}(m) = \frac{1}{\sqrt{\hat{R}_{xx}(0)\hat{R}_{yy}(0)}}\hat{R}_{xy}(m). \quad (3.2)$$

The highest absolute cross-correlation values were selected for each subject and motion combination. The distributions of the absolute cross correlation values for each accelerometer pair were compared to find the pair with the lowest cross correlation. The lowest cross correlation would mean that those two accelerometers collect the least similar information. Therefore, those two accelerometers would compose the most informative reference signal for the Kalman filter.

3.3 EMG signal processing

In this thesis, the same Kalman filtering and smoothing method was used that was proposed by Hostettler et al. (2018). However, instead of the IMU data, the EMG signal was used as a model of the motion artifact component. The EMG signal was extracted from the ECG signal by high-pass filtering. A Butterworth high-pass filter (Butterworth, 1930) with an order of four and a cutoff frequency of 70 Hz was designed. Butterworth filter is an infinite impulse response (IIR) filter, meaning that the output depends on both, past inputs and past outputs. Butterworth filter is also called maximally flat magnitude filter, since the frequency response in the passband has no ripple. However, the main disadvantage of the Butterworth filter is that the flatness is achieved at the expense of relatively wide transition region from passband to stopband. Moreover, the phase response of the Butterworth filter is slightly non-linear, which means that different frequency components might be shifted with a different amount in time. As a result, the waveform might be slightly changed.

The cutoff frequency of 70 Hz was chosen, since most of the cardiac signal power should be below it as described in Section 2.2.3. To overcome the problem of the non-linear phase response, the ECG signals were zero-phase filtered by forward-backward filtering them with Matlab's *filtfilt* function. In forward-backward filtering, the output sequence of forward-filtering is run backwards to the filter, resulting in no time delay of frequency components. The forward-backward filtering makes the total order of the filter double of the original order.

3.4 Adaptive Kalman filtering and smoothing

The baseline wander compensation algorithm proposed by Hostettler et al. (2018) consists of three steps: IMU attitude tracking, electrode motion estimation, and motion artifact reduction. In this thesis, the feasibility of using the EMG signal as a reference signal for the Kalman filter used in the motion artifact reduction is studied. The EMG signal is used as a motion reference signal as it is, without further processing. Therefore, when the EMG signal is used, only the motion artifact reduction step is applied. The first two steps, which use the IMU data to create the reference signal for the third step, are used only to reproduce the results of the previous study for comparison.

The three steps of the baseline wander compensation algorithm are pre-

Table 3.1: Parameter values used in Kalman filtering algorithm

Symbol	Description	Value
\mathbf{C}_a	Accelerometer noise covariance	\mathbf{I}_3
\mathbf{C}_m	Magnetometer noise covariance	\mathbf{I}_3
\mathbf{C}_v	Reference vector process noise covariance	$\Delta t_n \mathbf{I}_3$
α_0	Measurement noise adaption constant	1
γ	Outlier detection threshold	6
τ	Covariance adaptation time constant	1
M	Stationary detection sliding window length	100
κ	Stationary detection threshold	7.8
\mathbf{C}_p	Position pseudo measurement noise covariance	1×10^{-3}
L	Filter length	15
\mathbf{C}_q	Filter coefficients process noise covariance	1×10^{-5}
\tilde{C}_e	ECG noise covariance	0.5

sented in the following subsections. The parameter values used in the algorithms are listed in Table 3.1.

3.4.1 IMU attitude tracking

The local electrode motion is estimated with the attitude tracking algorithm introduced by Särkkä et al. (2015). The attitude tracker estimates the attitude of each IMU by tracking the gravity and magnetic field vectors in the local coordinate frames of the IMU. The measurement model for the IMU accelerometer can be written as

$$\mathbf{y}_{a,n} = \mathbf{g}_n^L + \mathbf{a}_n^L + \mathbf{w}_{a,n}, \quad (3.3)$$

where \mathbf{g}_n^L is the gravity vector, \mathbf{a}_n^L is the acceleration of the body, and $\mathbf{w}_{a,n} \sim N(\mathbf{0}, \mathbf{C}_a)$ is the measurement noise. The superscript L refers to the local coordinate frame. Likewise, the magnetometer measurement model is given by

$$\mathbf{y}_{m,n} = \mathbf{m}_n^L + \mathbf{b}_m + \mathbf{w}_{m,n}, \quad (3.4)$$

where \mathbf{m}_n^L is the magnetic field vector, \mathbf{b}_m is the magnetometer bias, and $\mathbf{w}_{m,n} \sim N(\mathbf{0}, \mathbf{C}_m)$ is the measurement noise. The magnetometer bias is assumed to be constant and estimated by using the conventional sphere fitting calibration approach presented by Kok and Schön (2016).

Moreover, the dynamic model describing the rotations of both the magnetic field and the gravity vectors is given by

$$\mathbf{r}_n = \mathbf{A}(\omega_n) \mathbf{r}_{n-1} + \mathbf{v}_n, \quad (3.5)$$

where

$$\mathbf{A}(\boldsymbol{\omega}_n) = \mathbf{I}_3 + \sin(|\boldsymbol{\omega}_n|\Delta t) \frac{[-\boldsymbol{\omega}_n]_{\times}}{|\boldsymbol{\omega}_n|} + (1 - \cos(|\boldsymbol{\omega}_n|\Delta t)) \frac{[-\boldsymbol{\omega}_n]_{\times}^2}{|\boldsymbol{\omega}_n|^2}, \quad (3.6)$$

where Δt_n is the sampling interval, \mathbf{r}_n denotes either the gravity vector \mathbf{g}_n^L or the magnetic field vector \mathbf{m}_n^L , $\boldsymbol{\omega}_n$ is the angular velocity from the gyroscope, and $\mathbf{v}_n \sim N(\mathbf{0}, \mathbf{C}_v)$ is the process noise. The notation $[\cdot]_{\times}$ is used for the cross product matrix.

Next, the gravity vector $\hat{\mathbf{g}}_n^L$ and the magnetic field vector $\hat{\mathbf{m}}_n^L$ are estimated. The estimates are obtained by running the Kalman filter and smoothing algorithm to the dynamic models (3.5) of the gravity and magnetic field vectors separately. This reference vector tracking algorithm is shown in Algorithm 1. The algorithm automatically adapts the measurement noise covariance if prominent body acceleration is detected.

Finally, the attitude matrix of the IMU in the global east-north-up (ENU) coordinate system can be estimated from the gravity and magnetic field vector estimates. First, the normal reference vector estimate can be obtained from the local gravity vector estimate as

$$\hat{\mathbf{e}}_n^{z,L} = \frac{\hat{\mathbf{g}}_n^L}{|\hat{\mathbf{g}}_n^L|}. \quad (3.7)$$

Second, the east reference vector estimate is given by

$$\hat{\mathbf{e}}_n^{x,L} = \frac{\hat{\mathbf{m}}_n^L \times \hat{\mathbf{e}}_n^{z,L}}{|\hat{\mathbf{m}}_n^L \times \hat{\mathbf{e}}_n^{z,L}|}. \quad (3.8)$$

Third, the north reference vector estimate is obtained from the cross product of the normal and east reference vectors:

$$\hat{\mathbf{e}}_n^{y,L} = \hat{\mathbf{e}}_n^{z,L} \times \hat{\mathbf{e}}_n^{x,L}. \quad (3.9)$$

These three estimates (Equations (3.7), (3.8) and (3.9)) then yield an estimate of the IMU attitude matrix that is given by

$$\hat{\mathbf{R}}_n^{LG} = [\hat{\mathbf{e}}_n^{x,L} \quad \hat{\mathbf{e}}_n^{y,L} \quad \hat{\mathbf{e}}_n^{z,L}]. \quad (3.10)$$

Algorithm 1 Robust Reference Vector Tracking Step (Särkkä et al., 2015):

1. Prediction:

$$\begin{aligned} \hat{\mathbf{r}}_n^- &= \mathbf{A}(\boldsymbol{\omega}_n) \hat{\mathbf{r}}_{n-1}, \\ \mathbf{C}_{\mathbf{r},n}^- &= \mathbf{A}(\boldsymbol{\omega}_n) \mathbf{C}_{\mathbf{r},n-1} \mathbf{A}(\boldsymbol{\omega}_n)^\top + \mathbf{C}_v. \end{aligned}$$

2. Measurement covariance adaption:

$$\begin{aligned}\alpha_n &= \exp(-\Delta t_n/\tau)\alpha_{n-1}, \\ \boldsymbol{\nu}_n &= \mathbf{y}_{j,n} - \hat{\mathbf{r}}_n^-, \\ \mathbf{S}_n &= \mathbf{C}_{r,n}^- + \mathbf{C}_j + \alpha_n \mathbf{I}_3.\end{aligned}$$

3. **if** $\boldsymbol{\nu}_n^\top \mathbf{S}_n^{-1} \boldsymbol{\nu}_n < \gamma$ **then**

4. Set

$$\begin{aligned}\alpha_n &= \alpha_0, \\ \mathbf{S}_n &= \mathbf{C}_{r,n}^- + \mathbf{C}_j + \alpha_n \mathbf{I}_3.\end{aligned}$$

5. **end if**

6. Measurement update:

$$\begin{aligned}\mathbf{K}_n &= \mathbf{C}_{r,n}^- \mathbf{S}_n^{-1}, \\ \hat{\mathbf{r}}_n &= \hat{\mathbf{r}}_n^- + \mathbf{K}_n \boldsymbol{\nu}_n, \\ \mathbf{C}_{r,n} &= \mathbf{C}_{r,n}^- - \mathbf{K}_n \mathbf{S}_n \mathbf{K}_n^\top.\end{aligned}$$

Algorithm 1 is applied to both accelerometer and magnetometer dynamic models independently. The superscript j in $\mathbf{y}_{j,n}$ and C_j is either a for accelerometer or m for magnetometer. α_0 is the measurement noise adaptation constant, γ is the outlier detection threshold, and τ is the covariance adaptation time constant.

3.4.2 Electrode motion estimation

For estimating the electrode motion, an inertial navigation model (Titterton and Weston, 2004) is used as the dynamic model for the Kalman filter. The model is given by

$$\mathbf{x}_n = \mathbf{F}_n \mathbf{x}_{n-1} + \mathbf{L}_n \hat{\mathbf{a}}_n. \quad (3.11)$$

In the model

$$\mathbf{x}_n = \begin{bmatrix} \mathbf{p}_n \\ \mathbf{v}_n \end{bmatrix}, \quad \mathbf{F}_n = \begin{bmatrix} 1 & \Delta t_n \\ 0 & 1 \end{bmatrix} \otimes \mathbf{I}_3, \quad \mathbf{L}_n = \begin{bmatrix} \frac{(\Delta t_n)^2}{2} \\ \Delta t_n \end{bmatrix} \otimes \mathbf{I}_3,$$

where \mathbf{p}_n denotes the position of the electrode, \mathbf{v}_n the velocity of the electrode, and \otimes the Kronecker product. $\hat{\mathbf{a}}_n$ is the IMU acceleration which is estimated

from the measured acceleration $\mathbf{y}_{a,n}$, the estimated local gravity vector $\hat{\mathbf{g}}_n^L$, and the attitude matrix $\hat{\mathbf{R}}_n^{LG}$ as

$$\hat{\mathbf{a}}_n = (\hat{\mathbf{R}}_n^{LG})^\top (\mathbf{y}_{a,n} - \hat{\mathbf{g}}_n^L), \quad (3.12)$$

and

$$\hat{\mathbf{a}}_n \sim N(\mathbf{a}_n, \mathbf{C}_{\hat{\mathbf{a}},n}), \quad (3.13)$$

where

$$\mathbf{C}_{\hat{\mathbf{a}},n} = (\hat{\mathbf{R}}_n^{LG})^\top (\mathbf{C}_{\hat{\mathbf{g}},n} + \mathbf{C}_a) \hat{\mathbf{R}}_n^{LG} \quad (3.14)$$

with $\mathbf{C}_{\hat{\mathbf{g}},n}$ being the covariance matrix of the local gravity vector estimate $\hat{\mathbf{g}}_n^L$.

Unfortunately, motion tracking systems typically suffer from the problem of position and velocity error growth due to, for example, the sensor bias. To reduce the position error growth, stationary phase detection is used along with pseudo measurement updates. The statistical test to detect the stationary phases is similar to one presented by Skog et al. (2010). First, the mean acceleration is calculated for a sliding window of length M :

$$\bar{\mathbf{a}}_n = \frac{1}{M} \sum_{m=0}^{M-1} \hat{\mathbf{a}}_{n-m}, \quad (3.15)$$

In stationary phases, the mean acceleration is distributed according to

$$\bar{\mathbf{a}}_n \sim N(\mathbf{0}, \mathbf{C}_{\bar{\mathbf{a}},n}), \quad (3.16)$$

where

$$\mathbf{C}_{\bar{\mathbf{a}},n} = \frac{1}{M^2} \sum_{m=0}^{M-1} \mathbf{C}_{\bar{\mathbf{a}},n-m}. \quad (3.17)$$

Second, the test statistic is formed:

$$\rho_n = \bar{\mathbf{a}}_n^\top \mathbf{C}_{\bar{\mathbf{a}},n}^{-1} \bar{\mathbf{a}}_n \quad (3.18)$$

which is distributed as

$$\rho_n \sim \chi^2(3). \quad (3.19)$$

The stationary detection threshold κ is chosen so that $\Pr\{\rho_n \leq \kappa\} = \alpha$ in the stationary phases.

Third, if a stationary phase is detected, a zero position pseudo measurement update is done. The measurement model for the pseudo measurement update is given by

$$\mathbf{y}_{p,n} = [\mathbf{I}_3 \quad \mathbf{0}] \mathbf{x}_n + \mathbf{w}_{p,n}, \quad (3.20)$$

where $\mathbf{y}_{p,n} = [0 \ 0 \ 0]^\top$ and $\mathbf{w}_{p,n} \sim N(\mathbf{0}, \mathbf{C}_p)$.

The modified Kalman filter with the conditional measurement updates is shown in Algorithm 2.

Algorithm 2 Motion Estimation Step (Hostettler et al., 2018)

1. Estimate $\hat{\mathbf{a}}_n$ and $\mathbf{C}_{\hat{\mathbf{a}},n}$

2. Prediction:

$$\begin{aligned}\hat{\mathbf{x}}_n^- &= \mathbf{F}_n \hat{\mathbf{x}}_{n-1} + \mathbf{L}_n \hat{\mathbf{a}}_n, \\ \mathbf{C}_{\hat{\mathbf{x}},n}^- &= \mathbf{F}_n \mathbf{C}_{\hat{\mathbf{x}},n-1} \mathbf{F}_n^\top + \mathbf{L}_n \mathbf{C}_{\hat{\mathbf{a}},n} \mathbf{L}_n^\top.\end{aligned}$$

3. Stationary detection:

$$\begin{aligned}\bar{\mathbf{a}}_n &= \bar{\mathbf{a}}_{n-1} + \frac{1}{M}(\hat{\mathbf{a}}_n - \hat{\mathbf{a}}_{n-M}), \\ \mathbf{C}_{\bar{\mathbf{a}},n} &= \mathbf{C}_{\bar{\mathbf{a}},n-1} + \frac{1}{M^2}(\mathbf{C}_{\hat{\mathbf{a}},n} - \mathbf{C}_{\hat{\mathbf{a}},n-M}), \\ \rho_n &= \bar{\mathbf{a}}_n^\top \mathbf{C}_{\bar{\mathbf{a}}}^{-1} \bar{\mathbf{a}}_n.\end{aligned}$$

4. **if** $\rho_n \leq \kappa$ **then**

5. Pseudo measurement update:

$$\begin{aligned}\hat{\mathbf{p}}_n^- &= \mathbf{G} \hat{\mathbf{x}}_n^-, \\ \mathbf{S}_n &= \mathbf{G} \mathbf{C}_{\hat{\mathbf{x}},n}^- \mathbf{G}^\top + \mathbf{C}_p, \\ \mathbf{K}_n &= \mathbf{C}_{\hat{\mathbf{x}},n}^- \mathbf{G}^\top \mathbf{S}_n^{-1}, \\ \hat{\mathbf{x}}_n &= \hat{\mathbf{x}}_n^- + \mathbf{K}_n(\mathbf{0} - \hat{\mathbf{p}}_n^-), \\ \mathbf{C}_{\hat{\mathbf{x}},n} &= \mathbf{C}_{\hat{\mathbf{x}},n}^- - \mathbf{K}_n \mathbf{S}_n \mathbf{K}_n^\top.\end{aligned}$$

6. **else**

7. Set

$$\begin{aligned}\hat{\mathbf{x}}_n &= \hat{\mathbf{x}}_n^-, \\ \mathbf{C}_{\hat{\mathbf{x}},n} &= \mathbf{C}_{\hat{\mathbf{x}},n}^-.\end{aligned}$$

8. **end if**

3.4.3 Motion artifact reduction

In the motion artifact reduction step, either the local position $\hat{\mathbf{p}}_n$, obtained from the previous step, or the EMG signal, obtained as described in Section 3.3, is used as a reference signal. The measurement model for the ECG signal is given by

$$y_{e,n} = s_{c,n} + s_{d,n} + w_{e,n}, \quad (3.21)$$

where $s_{c,n}$ is the cardiac signal, $s_{d,n}$ is the baseline wander disturbance, and $w_{e,n} \sim N(0, C_e)$ is the measurement noise.

Baseline wander disturbance component is assumed to have a time-varying correlation with the local motion of the electrode (Hostettler et al., 2018). In addition, the disturbance component is assumed to exhibit the correlation also with the EMG signal $y_{m,n}$ produced by the muscle movement. Hence, the motion artifact $s_{d,n}$ is modeled as filtered version of electrode displacements with time varying coefficients

$$s_{d,n} = \mathbf{H}_n \boldsymbol{\beta}_n \quad (3.22)$$

with either

$$\mathbf{H}_n = [1 \quad \hat{\mathbf{p}}_{1,n}^\top \quad \cdots \quad \hat{\mathbf{p}}_{1,n_L+1}^\top \quad \hat{\mathbf{p}}_{2,n}^\top \quad \cdots \quad \hat{\mathbf{p}}_{2,n-L+1}^\top], \quad (3.23)$$

if the local position is used as the reference signal, or

$$\mathbf{H}_n = [1 \quad \mathbf{y}_{m,n}^\top \quad \cdots \quad \mathbf{y}_{m,n_L+1}^\top], \quad (3.24)$$

if the EMG signal is used as the reference signal. In the equations, L is the filter length and $\boldsymbol{\beta}_n$ is a $(3L+1) \times 1$ vector of filter coefficients. The dynamic model of the filter coefficients is modeled as slowly time-varying random walk

$$\boldsymbol{\beta}_n = \boldsymbol{\beta}_{n-1} + \mathbf{q}_n, \quad (3.25)$$

where $\mathbf{q}_n \sim N(\mathbf{0}, \mathbf{C}_q)$ is the process noise.

Moreover, the ECG signal $s_{c,n}$ in (3.21) is merged into the measurement noise $w_{e,n}$. It yields to

$$y_{e,n} \approx \mathbf{H}_n \boldsymbol{\beta}_n + \tilde{w}_{e,n}, \quad (3.26)$$

where the unmodeled ECG signal in the measurement noise $\tilde{w}_{e,n}$ causes it to be non-Gaussian. However, it is assumed that $\tilde{w}_{e,n} \sim N(0, \tilde{C}_e)$, where the increase in the measurement noise covariance results from the unmodeled ECG signal.

Finally, a standard Kalman filter is used to estimate the coefficients $\boldsymbol{\beta}_n$ and consequently the unknown disturbance $s_{d,n}$. The motion compensated

ECG signal estimation $\hat{s}_{c,n}$ is obtained by reducing the disturbance estimate $\hat{s}_{d,n}$ from the measured ECG signal $y_{e,n}$. The Kalman filter algorithm is shown in Algorithm 3.

Algorithm 3 Motion Artifact Reduction Step (Hostettler et al., 2018)

1. Prediction:

$$\begin{aligned}\hat{\beta}_n^- &= \hat{\beta}_{n-1}, \\ \mathbf{C}_{\hat{\beta},n}^- &= \mathbf{C}_{\hat{\beta},n} + \mathbf{C}_q.\end{aligned}$$

2. Measurement update:

$$\begin{aligned}\hat{s}_{d,n} &= \mathbf{H}_n \hat{\beta}_n^-, \\ S_n &= \mathbf{H}_n \mathbf{C}_{\hat{\beta},n}^- \mathbf{H}_n^\top + \tilde{C}_e, \\ \mathbf{K}_n &= \mathbf{C}_{\hat{\beta},n}^- \mathbf{H}_n^\top S_n^{-1}, \\ \hat{\beta}_n &= \hat{\beta}_n^- + \mathbf{K}_n (y_{e,n} - \hat{s}_{d,n}), \\ \mathbf{C}_{\hat{\beta},n} &= \mathbf{C}_{\hat{\beta},n}^- - \mathbf{K}_n S_n \mathbf{K}_n^\top.\end{aligned}$$

3. Estimate ECG signal:

$$\hat{s}_{e,n} = y_{e,n} - \hat{s}_{d,n}.$$

3.5 Butterworth high-pass filtering

A conventional Butterworth high-pass filter (Butterworth, 1930) was used for baseline wander removal to compare the Kalman filter algorithm performance with a more traditional method (Lenis et al., 2017; Kaur and Singh, 2011; Chavan et al., 2008). There are several classical filtering methods used for baseline wander removal, but Butterworth filter is the most common choice.

A Butterworth filter with an order of four and a cutoff frequency of 0.5 Hz was designed. The cutoff frequency was chosen so that the baseline wander would be removed but the cardiac signal would be removed as little as possible. The spectral contents of ECG signal and baseline wander artifact are described in Sections 2.2.3 and 2.3, respectively. To overcome the problem of the non-linear phase response of the Butterworth filter, explained in Section 3.3, the raw ECG signals were zero-phase filtered by forward-backward filtering them with Matlab's *filtfilt* function.

3.6 Algorithm evaluation

The performance of the method was evaluated both in time domain and frequency domain. The characteristics of the filtered signals were compared to the characteristics of reference signal template representing a signal with no motion artifacts. Since there were no resting state reference measurements made by Hostettler et al. (2018), the reference signals for the template were extracted from the movement measurements by selecting sections where no baseline wander was visually observed. Three reference signals of 11.4 seconds duration were selected from all three leads separately. The reference signals were lowpass-filtered with 40 Hz cutoff frequency to obtain clean signals without EMG noise. Further, a reference power spectrum for frequency domain evaluation was determined by calculating the average spectrum of the three reference signals. First, the Fast Fourier Transforms (FFT) were calculated for the signals. Next, the single-sided spectra were estimated from the absolute FFT values. The average spectrum was determined by calculating the mean of the three spectra. The reference spectrum is a representation of a spectrum from a signal without motion artifacts. Therefore, the power of the spectrum is concentrated on the frequencies of the PQRSST waveform and the typical below 1 Hz frequencies of baseline wander have very low power.

A 11.4 seconds long section of each unprocessed and filtered signal was chosen for evaluation. The sections were chosen in a way that they expressed the most baseline wander in the unprocessed signal. First, the signal under evaluation was filtered with an IIR filter with the cutoff frequency of 0.7 Hz to remove all other information but the baseline. Next, the mean value of the baseline was calculated. To find the section with the most deviation from the mean value, the root mean square error (RMSE) from the mean was calculated for 11.4 second sections in intervals of 2.0 seconds. The RMSE was calculated as follows:

$$\text{RMSE} = \sqrt{\sum_{i=1}^n \frac{(\bar{y} - y_i)^2}{n}}, \quad (3.27)$$

where \bar{y} is the mean value, y_i are observed values and n is the number of observations. The section with the highest deviation was chosen for evaluation.

In order to make the signals from different subjects and motions comparable with the reference signal, all evaluation signals were normalized to have a mean 0 and standard deviation 1.

In frequency domain, the similarity between the power spectral density (PSD) distributions of filtered and reference signal was examined. The comparison was done by calculating the Kullback–Leibler (KL) divergence be-

tween the distributions. The PSDs of the signal sections under evaluation were estimated similarly as previously described for the template. The PSDs were handled as probability distributions. The KL divergence value for comparison of the evaluation signal and reference signal was calculated with equation

$$D_{KL}(P||Q) = \sum_{x \in X} P(x) \log \frac{P(x)}{Q(x)}, \quad (3.28)$$

where P is the PSD of the filtered evaluation signal and Q is the PSD of the reference signal. The closer the Kullback–Leibler divergence value is to zero, the more similar are the distributions.

Chapter 4

Results

This chapter presents the results obtained. The descriptions of the collected data is presented in Section 4.1 and of the resulting EMG signal in Section 4.2. The cross correlations of the IMUs are presented in Section 4.3. The results of the signal processing are shown in Section 4.4 and finally, the results of the algorithm evaluation in Section 4.5.

4.1 Collected data

In the clinical trials, a total of 20 subjects were measured, but the IMU data from all motion sensors was successfully recorded only for 11 subjects. However, for four of the measured subjects, the IMU data was missing only from LA. According to the results obtained in the IMU cross-correlation study, shown in Section 4.3, the IMU data from LA was not utilized in the signal processing. Therefore, the measurements missing only the IMU data from LA could still be used. Thus, the measurements from 15 subjects were processed and examined in this study.

An example of the measured ECG, during one subject performing the motion sequence 3, is given in Figure 4.1. All three leads express some baseline wander starting about at $t = 19$ s. The motion of bending towards the floor is performed twice, which is best observed from the two periods (between $t \approx 20$ s and $t \approx 23$ s as well as $t \approx 27$ s and $t \approx 29$ s) of notable EMG noise caused by the muscle contraction.

Figure 4.2 presents the same lead II ECG signal along with the acceleration data collected with all the five IMUs. The acceleration data shows as well that the motion starts at about $t = 19$ s. The motion is visible in all three channels (x, y, z) of all IMUs. However, the baseline wander still occurs even after the subject has finished the motion. It is notable that al-

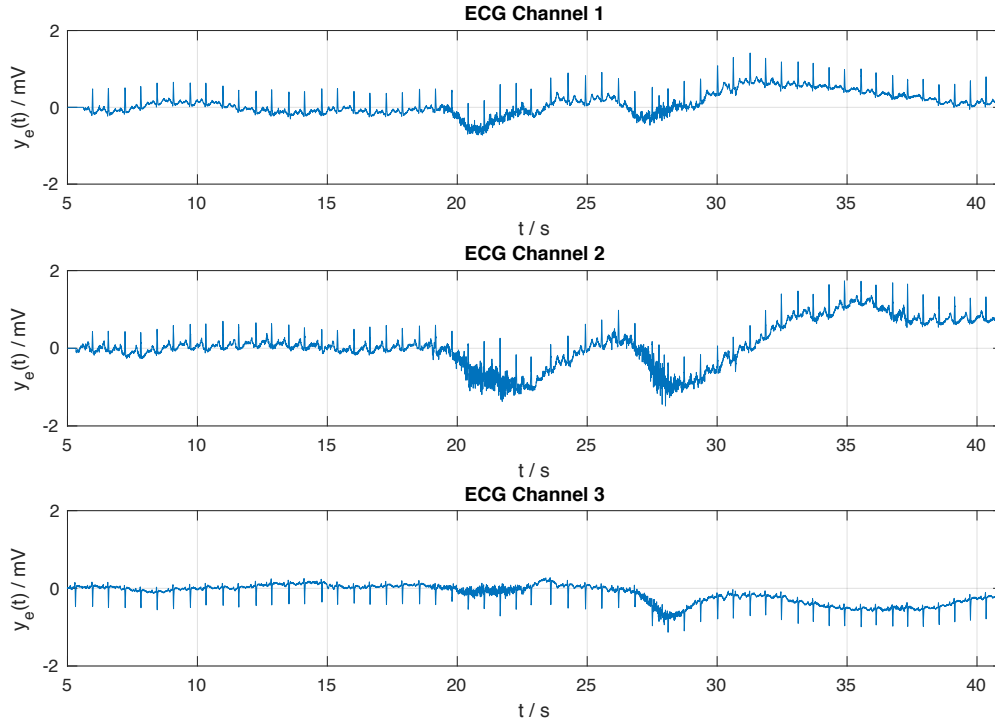


Figure 4.1: Example of the ECG signals from all three leads I, II, and V1 (channels 1, 2, and 3, respectively) measured during the motion sequence 3. Baseline wander as well as EMG noise visible in all three leads, starting from $t \approx 19$ s.

though the acceleration data looks very similar for both repetitions of the motion, the ECG signal reacts differently to the motion in both repetitions. For most of the subjects, all seven motion sequences caused visible artifacts, both baseline wander and muscle noise, in all three measured leads.

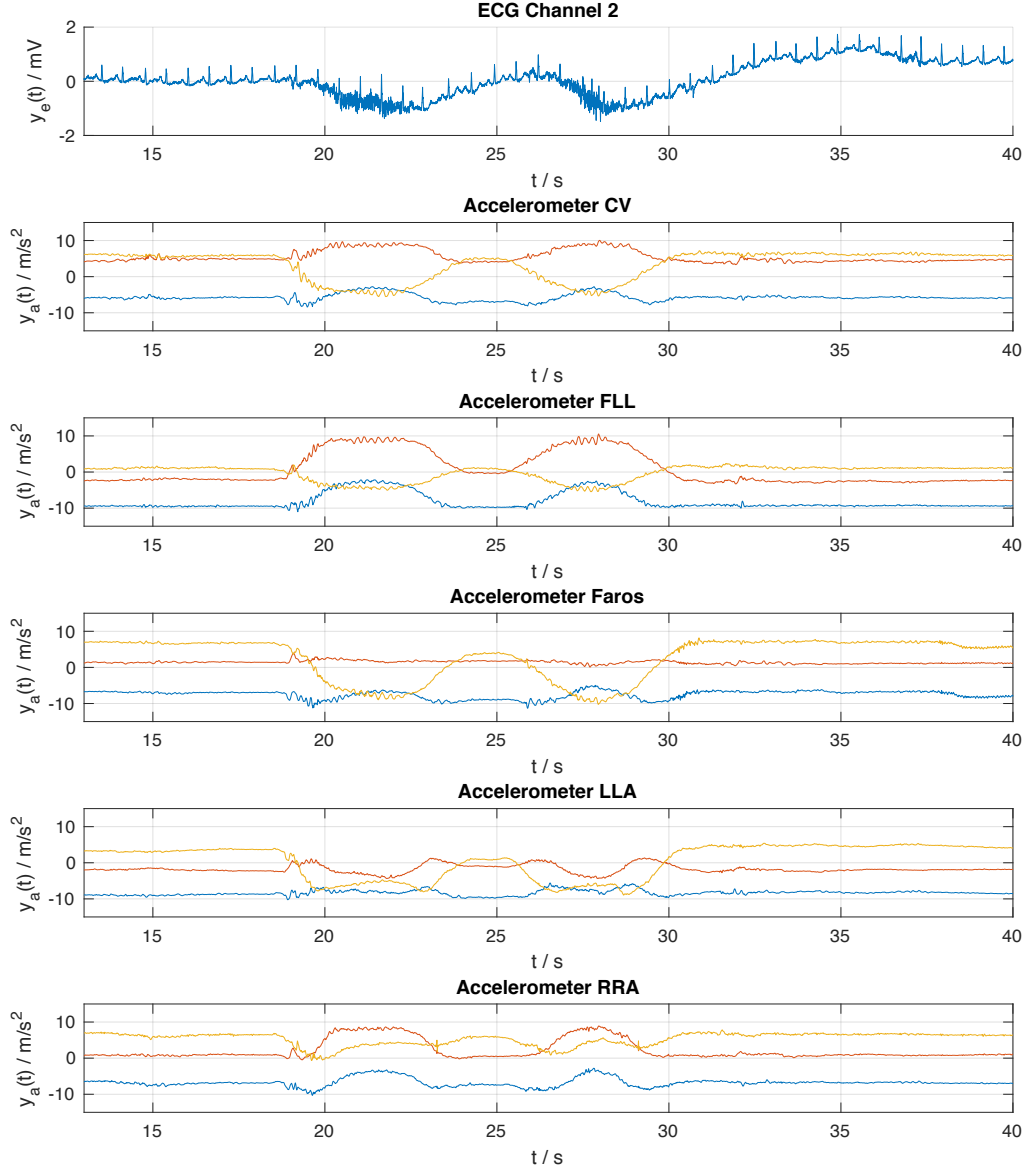


Figure 4.2: Example of the lead II ECG signal and all three channels (x, y, z) of the acceleration signals from all five IMUs measured during the motion sequence 3. The baseline wander (starting from $t \approx 19$ s) and the EMG noise (between $t \approx 20$ s and $t \approx 23$ s as well as $t \approx 27$ s and $t \approx 29$ s) detected in the ECG signal correspond to the motion detected with the IMUs.

4.2 EMG extraction

The EMG signal resulting from Butterworth high-pass filtering the ECG signal is shown in Figure 4.3 as well as the close-up view of the same signal in Figure 4.4. The EMG signal is presented in comparison with the raw ECG signal. It can be seen that the Butterworth filter has successfully removed the cardiac information from the ECG signal, preserving only the electric signal caused by the skeletal muscle activity. In addition, the baseline wander artifact has been removed since it appears at very low frequencies. The amplitude of the EMG signal might be slightly decreased as a result of the filtering.

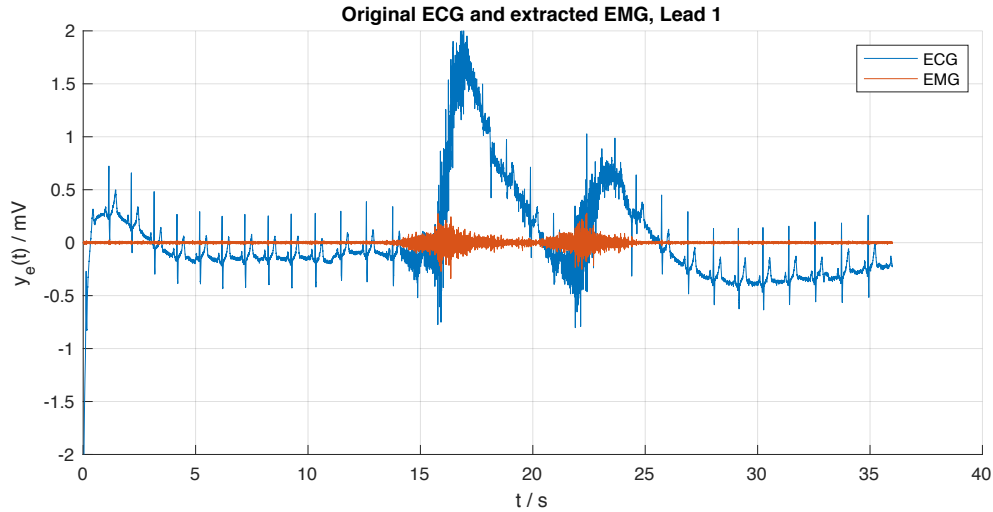


Figure 4.3: Comparison of the raw lead I ECG signal measured during the motion sequence 5 and the EMG signal extracted from the ECG by high-pass filtering. High-pass filtering has removed the cardiac information from the ECG signal but retained most of the electromyographic information.

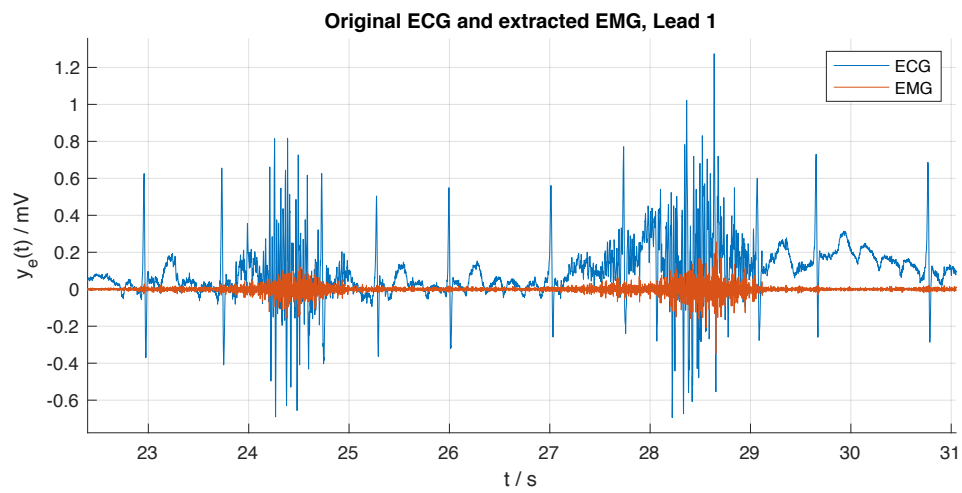


Figure 4.4: Close-up comparison of the raw lead I ECG signal measured during the motion sequence 2 and the EMG signal extracted from the ECG by high-pass filtering.

4.3 IMU cross correlations

The cross correlations between the IMU z -axis accelerations were calculated to find out if the number of IMUs used could be reduced. Figure 4.5 presents the boxplots of the absolute cross correlations for each accelerometer pair. The boxplots show that especially the accelerations of CV, LA, and RA correlate strongly with each other, thus collect overlapping data. The accelerations of LL and Faros have the lowest median of absolute correlation coefficients. They seem to collect the most divergent data. Therefore, those two IMUs are chosen to be used for the Kalman filter motion reference when processing the ECG signals with a reduced IMU set. The feasibility of using only LL and Faros IMUs was examined by comparing the output signals obtained with the lead-related reference signal and the reference signal from fixed IMUs. The output signals had almost no visible or measurable difference.

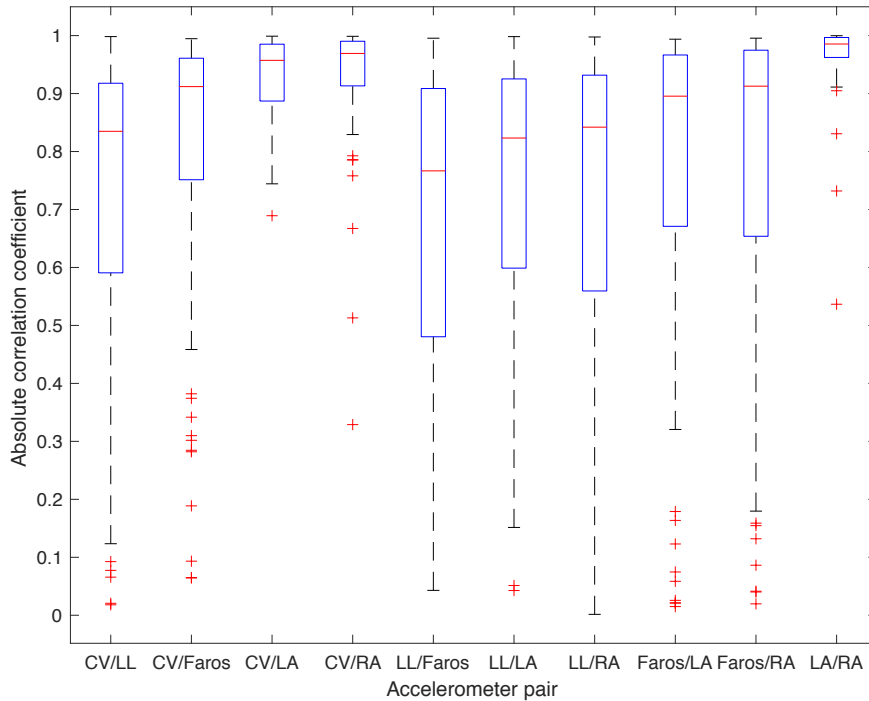


Figure 4.5: Boxplots showing the distributions of the absolute cross correlation coefficients of the z -axis accelerations for each IMU pair. The accelerations of LL and Faros have the lowest median of absolute correlation coefficients, while the accelerations of CV, LA, and RA correlate strongly with each other.

4.4 Signal processing results

A comparison of three filtering methods was performed: Kalman filtering with the EMG as a reference, Kalman filtering with the IMUs as a reference, and Butterworth high-pass filtering. Figure 4.6 shows an example comparison of the raw ECG signal and the ECG signal filtered using the EMG signal as a reference for motion. The signal is measured during the subject performing the motion sequence 5, raising hands. The comparison shows that most of the baseline wander has been removed. However, there is still little baseline wander left. The close-up of the phase with motion in Figure 4.7 shows that especially in the beginning of the steep climb of the baseline, the filtered baseline also rises little and then drops slightly below the zero-level before stabilizing. Furthermore, the comparison shows that the filtering process has slightly reduced some of the high frequency components but the EMG artifact has not been notably affected. The signal morphology seems to be well retained.

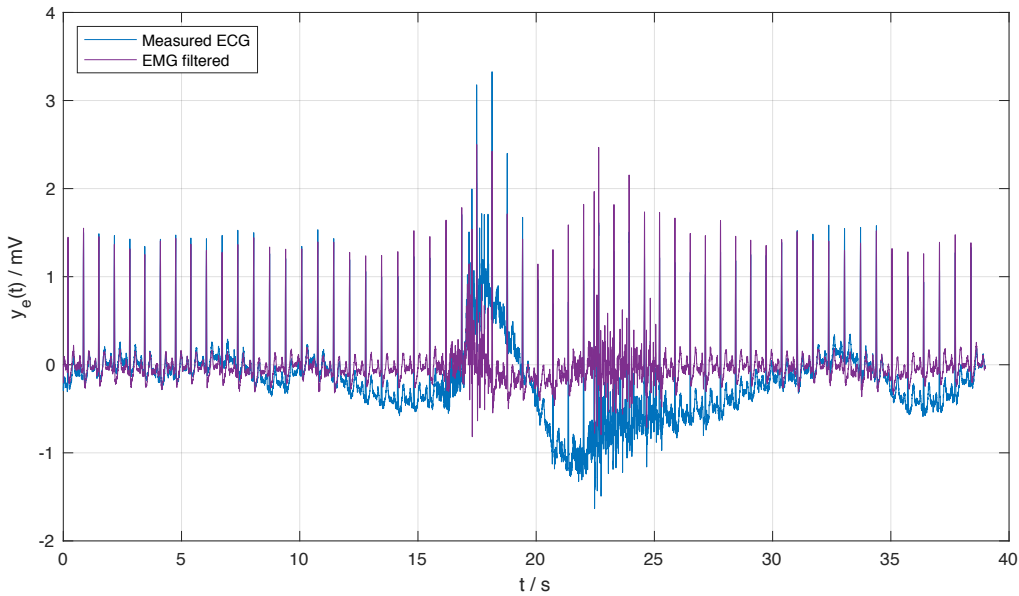


Figure 4.6: Comparison of the measured lead II ECG signal and the signal processed with EMG reference. The signal was measured during the motion sequence 5. Most of the baseline wander has been removed.

Figure 4.8 shows a close-up of the same signal from a phase with no motion and no significant baseline wander. The algorithm shows some weakness in

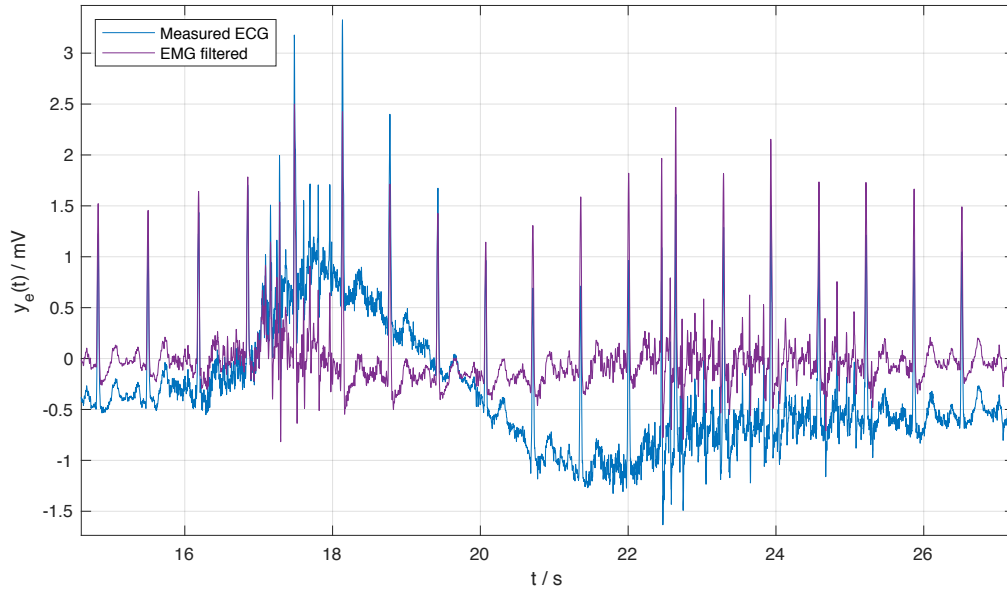


Figure 4.7: Close-up comparison of the measured lead II ECG signal and the signal processed with the EMG reference during a period with motion artifacts. The baseline of the processed signal slightly rises in the beginning of the step rise in the measured signal. The EMG has not been notably affected. The signal was measured during the motion sequence 5.

retaining the morphology when after each R-peak the level of the baseline drops slightly and then returns quickly back to normal. Moreover, it can be observed that the amplitudes of the R-peaks are slightly decreased. However, the alterations in the signal morphology are not substantial. The P-wave, the QRS complex and the T-wave are all clearly recognizable.

Finally, Figure 4.9 presents a comparison of processing the signal with the EMG reference and with the two other processing methods. It can be seen that the resulting signals are very similar from Kalman filtering with the IMU reference and from Kalman filtering with the EMG reference. The baseline of the Butterworth high-pass filtered signal fluctuates slightly less than the baselines of the Kalman filtered signals.

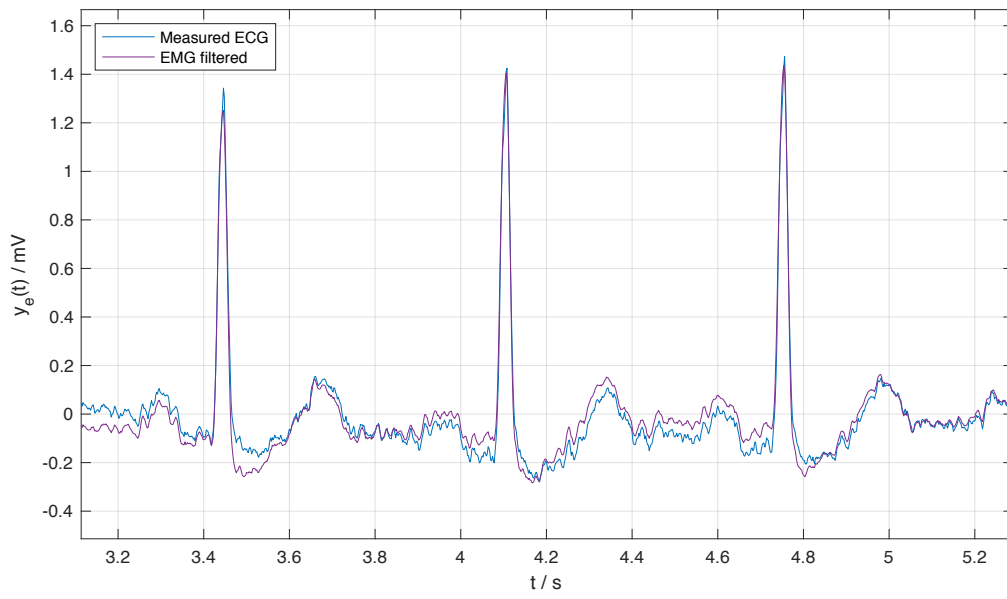


Figure 4.8: Comparison of the signal morphology in the measured lead II ECG signal and the signal processed with the EMG reference during a period without motion artifacts. The amplitudes of the R-peaks are slightly decreased and the baseline makes a small drop after the R-peaks, but mostly the morphology is well retained.

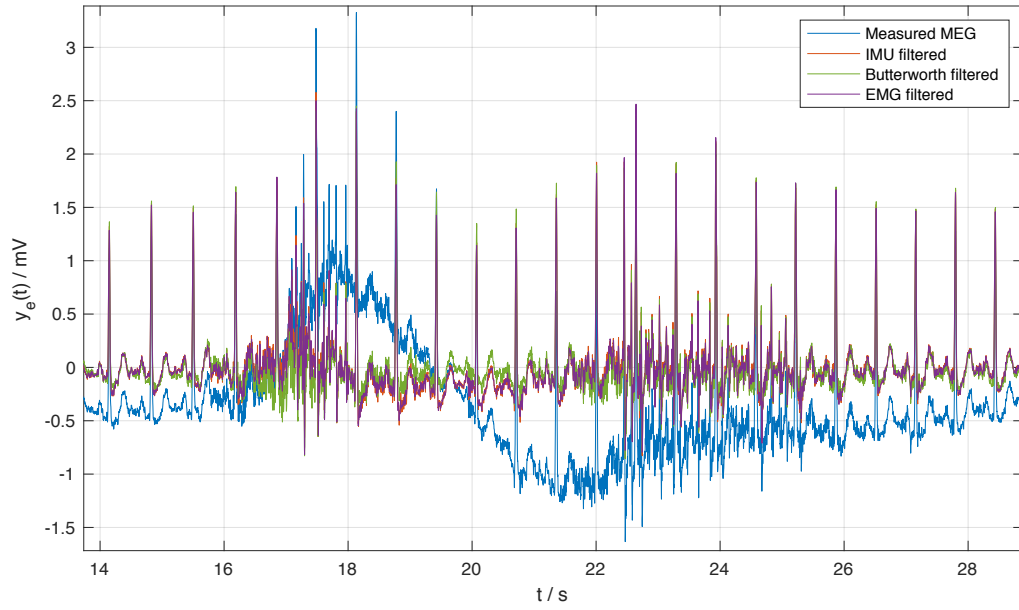


Figure 4.9: Comparison of the measured lead II ECG signal, the signal processed with the IMU reference, the signal processed with the Butterworth high-pass filter and the signal processed with the EMG reference during a period with motion artifacts. The methods using EMG and IMU references have performed very similarly. The baseline of the Butterworth filtered signal fluctuates slightly less than the other two. The signal was measured during the motion sequence 5.

4.5 Algorithm performance evaluation

The performance of the baseline wander reduction algorithm was evaluated in frequency domain by calculating the KL divergences between the PSD distributions of the processed signals and the reference PSD distribution. Figures 4.10, 4.11, and 4.12 provide a comparison of the KL divergences from the reference PSD for the raw ECG signals and the signals filtered with the different methods. Higher value indicates higher divergence with zero being the KL divergence of identical distributions. For all three leads, the signals processed with the EMG reference seem to have the lowest median KL divergence values as well as the narrowest distributions for all motions.

For evaluating how well the processing retains the ECG signal morphology, five comparisons of the filtered signals were shown to medical doctor Tuomas Lumikari. He assessed the effect of the signal processing to the signal interpretation: "Throughout patients all three compensation methods seem to be equally good to compensate baseline wander. This compensation looks good to me as a clinician in terms of baseline wander removal. There is no clinically important difference between methods yellow, pink, and green." The algorithms were anonymized to avoid any bias, hence the designations yellow, pink, and green referring to the plot color.

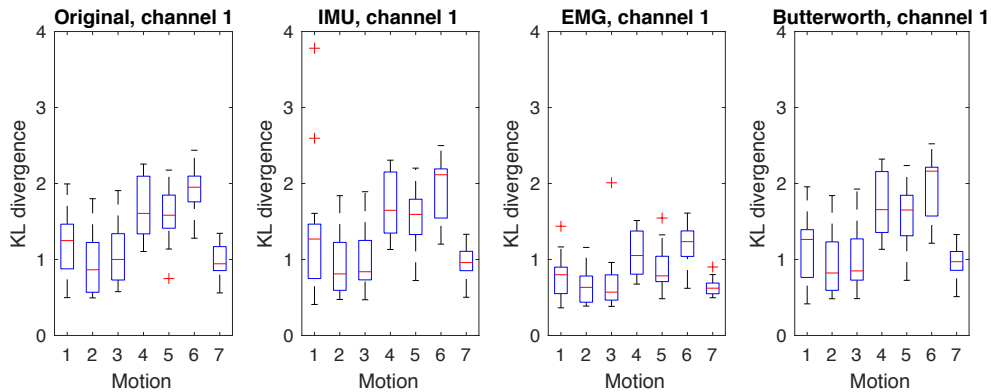


Figure 4.10: KL divergence boxplots between the measured or processed signal PSD distributions and the reference PSD distribution for lead I (channel 1) measurements. The boxplots are across all subjects for each motion sequence. The signals processed with the EMG reference have the lowest median KL divergence values as well as the narrowest distributions for each motion.

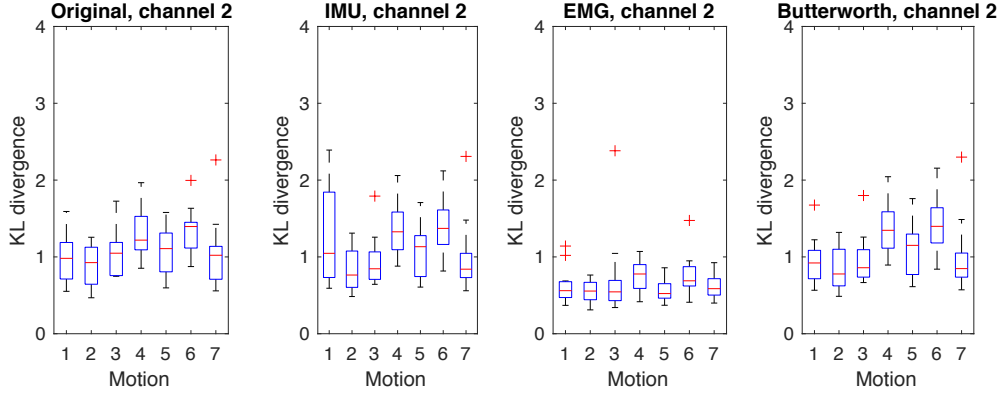


Figure 4.11: KL divergence boxplots between the measured or processed signal PSD distributions and the reference PSD distribution for lead II (channel 2) measurements. The boxplots are across all subjects for each motion sequence. The signals processed with the EMG reference have the lowest median KL divergence values as well as the narrowest distributions for each motion.

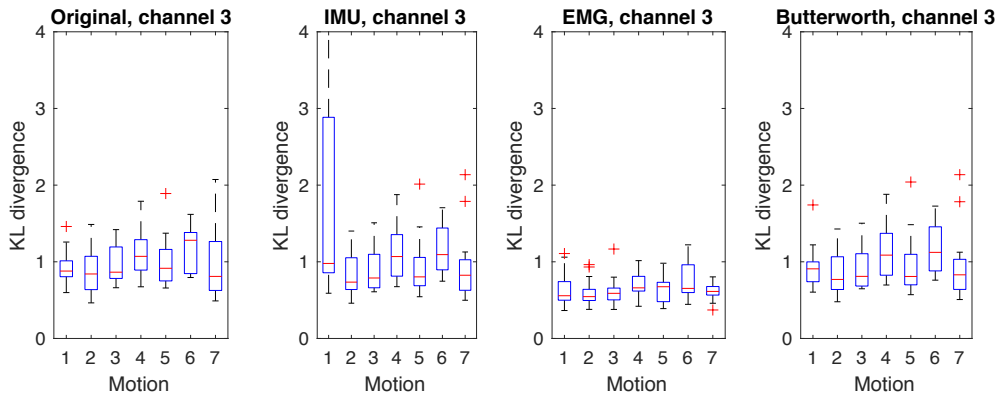


Figure 4.12: KL divergence boxplots between the measured or processed signal PSD distributions and the reference PSD distribution for lead V1 (channel 3) measurements. The boxplots are across all subjects for each motion sequence. The signals processed with the EMG reference have the lowest median KL divergence values as well as the narrowest distributions for each motion.

Chapter 5

Discussion and conclusions

The main aim of this thesis was to develop an ECG signal baseline wander reduction method that does not rely on additional sensors. A secondary goal was to study, if the Kalman filtering with IMU data reference could be performed with a reduced number of sensors.

Hostettler et al. (2018) had shown that the baseline wander could be successfully removed from the ECG signal using IMUs and Kalman filtering. In their study, an IMU was attached on top of each electrode. For each lead, the motion reference data was collected from the IMUs attached to those two electrodes recording the ECG lead. Thus, they utilize all the additional IMU sensors. In this thesis, a cross correlation study for the accelerometers was performed. The examination suggests that the accelerometers produce correlating data, meaning that some of them are redundant. The results are in accordance with the findings of Pyysing (2018), in which the correlation between the acceleration data and ECG were more dependent on the type of movement than on the location of the accelerometer. According to these results, the artifact reduction could be effectively performed with only two IMUs. The comparison of using the lead-related IMU data as a reference and using the data from the fixed two (LL and Faros) IMUs as a reference showed that they result in very similar output signals. The observation confirms the feasibility of using a reduced number of IMUs as a source for the motion reference signal.

The examination of the data collected in the clinical trial showed that typically the EMG noise occurred at the same time than the baseline wander as well as the motion detected with the IMUs. This finding implicates that the EMG signal could be used as a motion indicating reference signal for the Kalman filter. Furthermore, a successful extraction of the EMG signal from the ECG signal was achieved by forward-backward Butterworth high-pass filtering. The filtering slightly decreased the amplitude of the EMG signal,

but the signal was considered to contain enough information of the motion.

The feasibility of using the EMG signal as the motion reference for the Kalman filter was evaluated by running the baseline compensation algorithm on the collected clinical data. Visually evaluated, it seems that most of the baseline wander was removed. The filter did not notably affect the EMG noise. There were proportions of very scant baseline wander left, especially in the beginnings of the significant motion artifacts. Nevertheless, the remaining baseline wander was so scant that it does not substantially hinder the interpretation of the ECG signal. The remaining slight fluctuations of the baseline could be removed by adjusting the value of the algorithm parameter \mathbf{C}_q (process noise covariance of the coefficients β_n). However, it would also substantially affect the morphology of the ECG signal that is critically important in clinical interpretation of ECG. The closer examination of the results showed that with these parameter values the processed signal is slightly altered but the ECG morphology is not too much affected. The amplitude of the R-peak is slightly decreased and the baseline makes a small drop after each R-peak. However, the alterations in the morphology are so minor that they do not significantly affect the clinical interpretation of the signal. The P-wave, QRS-complex and T-wave are clearly observable. Moreover, the comments from doctor Lumikari confirmed that the processed signal has retained its diagnostic relevance.

The output signals obtained using the EMG signal as a motion reference were very similar with the ones obtained using the IMU data as a motion reference. Moreover, they are in accordance with the results Hostettler et al. (2018) found using the IMU data as a motion reference. In a visual comparison, both Kalman filter methods and the Butterworth high-pass filtering seemed to have performed equally well in baseline wander reduction. The equally good performance was qualitatively verified by doctor Lumikari. Even the Butterworth filter did not seem to alter the signal morphology significantly. This might be due to the high enough heart rates of the subjects during the measurements. With lower heart rate the spectral content of the ECG signal would include components of lower frequencies. However, despite the fair performance in this thesis, it is generally accepted that the Butterworth filter has limitations in ECG signal processing.

In addition to the visual evaluation, the performance of the baseline wander reduction algorithm was evaluated quantitatively in frequency domain. KL divergences were calculated between the PSD distributions of the signals processed with different methods and the reference PSD distribution. The comparison of the KL divergence boxplots revealed that the Kalman filter using the EMG reference signal attained the lowest KL divergences for all leads and all motions. Since the reference PSD presents the frequency content

of an ECG signal with very little baseline wander, the low KL divergences would indicate that the method using the EMG motion reference would perform even better than the other methods in removing the low frequency baseline wander. Furthermore, another possible reason for the method using the EMG motion reference gaining lower KL divergences, is the slight reduction of the higher frequency components. Since the reference signals were lowpass-filtered to have a clean signal, the reference PSD should also contain little high frequency components, hence causing the similarity.

However, the statistical significance of the difference in KL divergences could not be proven due to the small and possibly unbalanced data sets. Another major challenge in the quantitative evaluation of the algorithm was the lack of resting state measurements. Since the measurements were conducted only during the subjects performing motions, it was not possible to find a period with no baseline wander for each subject. The shapes, durations and amplitudes of the ECG signal waves and peaks vary between subjects. Therefore, each subject would need its own resting state measurement to work as a reference in order to perform reliable quantitative evaluation in time domain. Given that the shapes of the waves as well as the heart rate naturally affect the frequency content too, the evaluation in frequency domain would also be more accurate with individualized reference frequency spectra. In addition, it would improve the understanding of the relation between the motion artifacts and the motions if the timings of the motions in the measurements would be saved and reported.

A common way to study the performance of an filtering algorithm is adding generated noise to a clean signal and then comparing the filtered signal to the clean signal. In this case, that procedure was not possible since the EMG artifact itself was utilized as the reference signal for the filter and the assumed correlation between the EMG and the baseline wander was a requirement for the method to work.

As a conclusion, the use of the extracted EMG signal as a motion reference signal for the Kalman filter in baseline wander reduction in ECG seems feasible. The method performed equally well with the method using IMU data as a motion reference signal. The eligibility of the processed signals for the diagnostic interpretation was confirmed by a clinical doctor. In other words, it appears that the reduction of the baseline wander in the ECG signal could be achieved without any additional sensors. That would enable not only the measurement device to be lighter, cheaper, and less complex, but also the measurement to be more convenient for the patient. However, the algorithm performance could only be evaluated visually and in the frequency domain. More reliable quantitative evaluations would need a recording of proper resting state reference signals. For further improvements, the feasibility of the

real-time processing could be studied. In addition, the performance of the method used in this thesis was not studied on baseline wander caused by other sources than motion. The baseline wander artifact can also originate from, for example, pulling the wires attached to the electrodes or by pressure changes on the electrodes. This kind of artifact is not related to either EMG or acceleration.

References

- Ahmad, N., Ghazilla, R. A. R., Khairi, N. M., and Kasi, V. (2013). Reviews on various inertial measurement unit (IMU) sensor applications. *International Journal of Signal Processing Systems*, 1(2):256–262.
- AlGhatrif, M. and Lindsay, J. (2012). A brief review: history to understand fundamentals of electrocardiography. *Journal of Community Hospital Internal Medicine Perspectives*, 2(1).
- Baig, M., Gholamhosseini, H., and Connolly, M. (2013). A comprehensive survey of wearable and wireless ECG monitoring systems for older adults. *Medical & biological engineering & computing*, 51(5):485–495.
- Barold, S. (2003). Willem Einthoven and the birth of clinical electrocardiography a hundred years ago. *Cardiac electrophysiology review*, 7(1):99–104.
- Butterworth, S. (1930). On the theory of filter amplifiers. *Wireless Engineer*, 7(6):536–541.
- Chavan, M., Agarwala, R., and Uplane, M. (2008). Suppression of baseline wander and power line interference in ECG using digital IIR filter. *International journal of circuits, systems and signal processing*, 2(2):356–365.
- Crawford, J. and Doherty, L. (2011). *Practical Aspects of ECG Recording*. MK Update Ltd, 1st edition.
- European Stroke Organisation (ESO) (2008). Guidelines for management of ischaemic stroke and transient ischaemic attack 2008. *Cerebrovascular diseases*, 25(5):457–507.
- Grond, M., Jauss, M., Hamann, G., Stark, E., Veltkamp, R., Nabavi, D., Horn, M., Weimar, C., Köhrmann, M., Wachter, R., Rosin, L., and Kirchhof, P. (2013). Improved detection of silent atrial fibrillation using 72-hour Holter ECG in patients with ischemic stroke: a prospective multicenter cohort study. *Stroke*, 44(12):3357–3364.

- Gumbinger, C., Krumsdorf, U., Veltkamp, R., Hacke, W., and Ringleb, P. (2012). Continuous monitoring versus HOLTER ECG for detection of atrial fibrillation in patients with stroke. *European Journal of Neurology*, 19(2):253–257.
- Higgins, P., MacFarlane, P. W., Dawson, J., McInnes, G. T., Langhorne, P., and Lees, K. R. (2013). Noninvasive cardiac event monitoring to detect atrial fibrillation after ischemic stroke: a randomized, controlled trial. *Stroke*, 44(9):2525–2531.
- Hostettler, R., Lumikari, T., Palva, L., Nieminen, T., and Särkkä, S. (2018). Motion artifact reduction in ambulatory electrocardiography using inertial measurement units and Kalman filtering. In *21st International Conference on Information Fusion (FUSION), Cambridge, UK, July 2018*, pages 1–8. IEEE.
- Jabaudon, D., Sztajzel, J., Sievert, K., Landis, T., and Sztajzel, R. (2004). Usefulness of ambulatory 7-day ECG monitoring for the detection of atrial fibrillation and flutter after acute stroke and transient ischemic attack. *Stroke*, 35(7):1647–1651.
- Kalman, R. (1960). A new approach to linear filtering and prediction problems. *Transactions of the ASME, Journal of Basic Engineering*, 83(1):35–45.
- Katz, A. (2011). *Physiology of the Heart*. Lippincott Williams & Wilkins Health, 5th edition.
- Kaur, M. and Singh, B. (2011). Comparison of different approaches for removal of baseline wander from ECG signal. In *Proceedings of the International Conference & Workshop on Emerging Trends in Technology*, pages 1290–1294.
- Kempe, V. (2011). *Inertial MEMS: Principles and Practice*. Cambridge University Press.
- Kok, M. and Schön, T. (2016). Magnetometer calibration using inertial sensors. *IEEE Sensors Journal*, 16(14):5679–5689.
- Kovvali, N., Banavar, M., and Spanias, A. (2014). *An introduction to Kalman filtering with MATLAB examples*. Morgan & Claypool, 1st edition.
- Lenis, G., Pilia, N., Loewe, A., Schulze, W., and Dössel, O. (2017). Comparison of baseline wander removal techniques considering the preservation of

- ST changes in the ischemic ECG: a simulation study. *Computational and mathematical methods in medicine*, 2017.
- Mason, L. (2002). *Signal processing methods for non-invasive respiration monitoring*. PhD thesis, University of Oxford.
- Mneimneh, M., Yaz, E., Johnson, M., and Povinelli, R. (2006). An adaptive Kalman filter for removing baseline wandering in ECG signals. In *2006 Computers in Cardiology*, pages 253–256. IEEE.
- Murthy, V., Grove, T., Harvey, G., and Haywood, L. (1978). Clinical usefulness of ECG frequency spectrum analysis. In *The Second Annual Symposium on Computer Application in Medical Care, 1978. Proceedings.*, pages 610–612. IEEE.
- Orphanidou, C. (2018). *Signal Quality Assessment in Physiological Monitoring: State of the Art and Practical Considerations*. Springer, 1st edition.
- Pyysing, A. (2018). Movement artifacts in electrocardiography. Master’s thesis, Aalto University School of Electrical Engineering.
- Rodríguez-Martín, D., Pérez-López, C., Samà, A., Cabestany, J., and Català, A. (2013). A wearable inertial measurement unit for long-term monitoring in the dependency care area. *Sensors*, 13(10):14079–14104.
- Sameni, R., Shamsollahi, M., Jutten, C., and Babaie-Zade, M. (2005). Filtering noisy ECG signals using the extended Kalman filter based on a modified dynamic ECG model. In *Computers in Cardiology, 2005*, pages 1017–1020. IEEE.
- Sayadi, O. and Shamsollahi, M. (2008). ECG denoising and compression using a modified extended Kalman filter structure. *IEEE Transactions on Biomedical Engineering*, 55(9):2240–2248.
- Skog, I., Händel, P., Nilsson, J.-O., and Rantakokko, J. (2010). Zero-velocity detection — an algorithm evaluation. *IEEE transactions on biomedical engineering*, 57(11):2657–2666.
- Strootbandt, R., Barold, S., and Sinnaeve, A. (2016). *ECG from Basics to Essentials : Step by Step*. Hoboken: John Wiley & Sons, 1st edition.
- Sweeney, K. T., Ward, T. E., and McLoone, S. F. (2012). Artifact removal in physiological signals – practices and possibilities. *IEEE transactions on information technology in biomedicine*, 16(3):488–500.

- Särkkä, S. (2013). *Bayesian Filtering and Smoothing*. Cambridge University Press, 1st edition.
- Särkkä, S., Tolvanen, V., Kannala, J., and Rahtu, E. (2015). Adaptive Kalman filtering and smoothing for gravitation tracking in mobile systems. In *2015 International Conference on Indoor Positioning and Indoor Navigation (IPIN)*, pages 1–7. IEEE.
- Sörnmo, L. and Laguna, P. (2005). *Bioelectrical Signal Processing in Cardiac and Neurological Applications*. Elsevier, 1st edition.
- Titterton, D. and Weston, J. (2004). *Strapdown Inertial Navigation Technology*. The Institution of Electrical Engineers.
- Tobergte, A., Pomarlan, M., and Hirzinger, G. (2009). Robust multi sensor pose estimation for medical applications. In *2009 IEEE/RSJ International Conference on Intelligent Robots and Systems*, pages 492–497. IEEE.
- Tortora, G. and Derrickson, B. (2017). *Tortora’s principles of anatomy physiology*. Hoboken: John Wiley & Sons, 15th edition.
- Trobec, R., Tomašić, I., Rashkovska, A., Depolli, M., and Avbelj, V. (2018). *Body Sensors and Electrocardiography*. Springer International Publishing.
- Vullings, R., Vries, B. D., and Bergmans, J. (2010). An adaptive Kalman filter for ECG signal enhancement. *IEEE transactions on biomedical engineering*, 58(4):1094–1103.
- Waller, A. (1887). A demonstration on man of electromotive changes accompanying the heart’s beat. *The Journal of physiology*, 8(5):229–234.
- Webster, J. (2010). *Medical Instrumentation : Application and Design*. Hoboken, NJ :John Wiley Sons, 4th edition.
- Welch, G. and Bishop, G. (1995). An introduction to the Kalman filter. Technical Report TR 95-041, University of North Carolina.
- Wilson, F., Johnston, F., Macleod, A., and Barker, P. (1934). Electrocardiograms that represent the potential variations of a single electrode. *American Heart Journal*, 9(4):447–458.
- Wolf, P. A., Abbott, R. D., and Kannel, W. B. (1991). Atrial fibrillation as an independent risk factor for stroke: the Framingham Study. *Stroke*, 22(8):983–988.